Unravelling the regulation pathway of photosynthetic AB-GAPDH

Unravelling the regulation pathway of photosynthetic AB-GAPDH

Roberto Marotta[a,1], Alessandra Del Giudice[b,1], Libero Gurrieri[c], Silvia Fanti[d], Paolo Swuec[e], Luciano Galantini[b], Giuseppe Falini[d], Paolo Trost[c], Simona Fermani[d,*], Francesca Sparla[c,*]

[a]Electron Microscopy Facility (EMF), Italian Institute of Technology (IIT), 16163 Genova, Italy,

[b]Department of Chemistry, University of Rome Sapienza, 00185 Rome, Italy,

[c]Department of Pharmacy and Biotechnology–FaBiT, University of Bologna, 40126 Bologna, Italy,

[d]Department of Chemistry G. Ciamician, University of Bologna, 40126 Bologna, Italy,

[e]Biosciences Department, University of Milan, 20133 Milan, Italy,

[f]Interdepartmental Centre for Industrial Research Health Sciences & Technologies,University of Bologna, 40064 Bologna, Italy.

*Corresponding email: simona.fermani@unibo.it; francesca.sparla@unibo.it.

[1]These authors equally contributed to this work

This manuscript is dedicated to Emeritus Prof. Alberto Ripamonti

Synopsis The regulation of the heteromeric form of photosynthetic glyceraldehyde 3-phosphate dehydrogenase (AB-GAPDH) depends on the oscillation between a fully active heterotetramer (A_2B_2) and inhibited oligomers. Experimental evidence demonstrates that inhibition of spinach AB-GAPDH depends on the formation of dimers, tetramers or pentamers of A_2B_2-modules, linked together by C-terminal extensions (CTE) of B-subunits that extend from one modular tetramer and occupy two active sites of the adjacent one.

Abstract Oxygenic phototrophs perform carbon fixation through the Calvin–Benson cycle. Different mechanisms adjust the cycle and the light-harvesting reactions to rapid environmental changes. Photosynthetic glyceraldehyde 3-phosphate dehydrogenase (GAPDH) is a key enzyme of the cycle. In land plants, different photosynthetic GAPDHs exist: the most abundant isoform formed by heterotetramers A_2B_2 and the less abundant homotetramer A_4. Regardless of the subunit composition, GAPDH is the major consumer of photosynthetic NADPH and its activity is strictly regulated. While A_4-GAPDH is regulated by CP12, AB-GAPDH is autonomously regulated through the C-terminal extension (CTE) of B-subunits. Reversible inhibition of AB-GAPDH occurs via oxidation of a cysteine pair located in the CTE, and substitution of NADP(H) with NAD(H) in the cofactor binding site. These combined conditions lead to a change in the oligomerization state and enzyme inhibition. SEC-SAXS and single-particle cryoEM analysis were applied to disclose the structural basis of this regulatory mechanism. Both approaches revealed that spinach $(A_2B_2)_n$-GAPDH oligomers with n=1, 2, 4 and 5 co-

exist in a dynamic system. B-subunits mediate the contacts between adjacent tetramers in A_4B_4 and A_8B_8 oligomers. The CTE of each B-subunit penetrates into the active site of a B-subunit of the adjacent tetramer, which in turn moves its CTE in the opposite direction, effectively preventing the binding of the substrate 1,3-bisphosphoglycerate in the B-subunits. The whole mechanism is made possible, and eventually controlled, by pyridine nucleotides. In fact, NAD(H), by removing NADP(H) from A-subunits, allows the entrance of the CTE in B-subunit active site hence stabilizing inhibited oligomers.

Keywords: Photosynthesis; Redox regulation; Cryo-electron microscopy; Small angle X-ray scattering.

1. Introduction

Oxygenic photosynthesis sustains almost all life on Earth reducing carbon dioxide to carbohydrates while photo-oxidizing water to oxygen. The photosynthetic electron transport chain, strictly dependent on light, provides energy (ATP) and reducing power (NADPH) for the carbon fixation reactions. By consuming ATP and NADPH, carbohydrates are produced from CO_2 by the Calvin-Benson cycle (Bassham *et al.*, 1950; Michelet *et al.*, 2013; Johnson, 2016; Gurrieri *et al.*, 2021). Despite the historical distinction between the two phases of photosynthesis, the entire process occurs during the day through a complex and diversified regulatory system that harmonizes the rate of carbon fixation with the rate of conversion of light energy into chemical energy (Scheibe & Dietz, 2012; Minagawa & Tokutsu, 2015; Heyneke & Fernie, 2018). Thioredoxins (TRXs) represent one of the wake-up calls of the Calvin-Benson cycle at dawn. Through the TRX/ferredoxin system, part of the reducing power originated by the photosystem I induces the activation of the cycle in a TRX dependent manner (Huppe *et al.*, 1990; Buchanan, 1991; Nikkanen & Rintamäki, 2019). In land plants, phosphoribulokinase (PRK) (Brandes *et al.*, 1996; Gurrieri *et al.*, 2019; Yu *et al.*, 2020), fructose 1,6-bisphosphatase (FBPase) (Chiadmi, 1999; Gütle *et al.*, 2016), sedoheptulose-1,7-bisphosphatase (SBPase) (Gütle *et al.*, 2016) and the AB-isoform of glyceraldehyde 3-phosphate dehydrogenase (GAPDH) are direct targets of TRXs that by reduction of a disulfide bond activate the enzymes (Wolosiuk & Buchanan, 1978; Sparla *et al.*, 2002). GAPDH catalyzes the only reducing step of the Calvin-Benson cycle and is the major consumer of the photosynthetically produced NADPH. Two isoforms of photosynthetic GAPDH coexist in the chloroplast stroma of land plants: a homotetramer exclusively made of A subunits, and a heterotetramer containing both A and B-subunits (Scagliarini *et al.*, 1998; Gurrieri *et al.*, 2021) that can form higher order oligomers (Pupillo & Piccari, 1975; Buchanan & Wolosiuk, 1976). The structure of A_4- and A_2B_2-GAPDH is similar and highly conserved among GAPDHs (Fermani *et al.*, 2001, 2007). Although the regulation of both isoforms occurs by interaction with CP12 and PRK, AB-GAPDH shows an additional autonomous regulation (Carmo-Silva *et al.*, 2011; Gurrieri *et al.*, 2021). CP12 is a small conditionally disordered protein containing two pairs of conserved cysteines (Reichmann & Jakob, 2013; Launay *et*

al., 2018). The C-terminal pair, with a midpoint redox potential ($E_{m,7.9}$) of -352 mV, binds GAPDH, while the N-terminal disulfide characterized by a less negative potential ($E_{m,7.9}$ = -326 mV), recruits PRK into the complex (Gurrieri *et al.*, 2021; Marri *et al.*, 2010). Recently, the structure of A_4-GAPDH/CP12/PRK complex has been solved, enlightening the molecular mechanisms involved in complex formation and redox regulation (McFarlane *et al.*, 2019; Yu *et al.*, 2020). AB-GAPDH performs the CP12-independent regulation through the presence of a 30 amino acid tail specific to the B-subunit that contains a pair of cysteines close enough to form a disulfide bridge (Scheibe *et al.*, 1996; Sparla *et al.*, 2002; Fermani *et al.*, 2007; Gurrieri *et al.*, 2021). This C-terminal extension (CTE) is highly similar in sequence (~ 87% of identity) to the C-terminal region of CP12 and it has been proposed that the B-subunit results from the fusion between the A-subunit and the C-terminal half of CP12 (Wedel & Soll, 1998; Petersen *et al.*, 2006; Trost *et al.*, 2006; Gurrieri *et al.*, 2021). AB-GAPDH exhibits its own propensity to vary the oligomeric state from active heterotetramers to inhibited hexadecamers (Pupillo & Piccari, 1975; Scheibe *et al.*, 1996; Baalmann *et al.*, 1996; Howard *et al.*, 2008). The transition between the oligomeric states depends not only on the redox state of the CTE, but also on the type of cofactor (NADP(H) or NAD(H)) and on the substrate 1,3-bisphosphoglycerate (BPGA) availability (Sparla *et al.*, 2002, 2005). The convergence of several regulatory inputs on a single enzyme make its study challenging and suggests a central role of the enzyme in the overall regulation of the carbon flux through the Calvin-Benson cycle. As mentioned above, AB-GAPDH is regulated by thioredoxins, BPGA and pyridine nucleotides. Recently, it has been suggested that these regulators act in a coordinated manner, as supported by in vivo measurements indicating a kinetic constrain on the redox control of AB-GAPDH (Baalmann *et al.*, 1995; Zimmer *et al.*, 2021). That means that thioredoxin-dependent regulation of AB-GAPDH is affected over time by the availability of the substrates (Zimmer *et al.*, 2021). With the aim of disclosing the molecular mechanism that drives the oligomerization of AB-GAPDH, here we report a multi-approach structural study of the spinach AB-GAPDH system by small angle X-ray scattering coupled with size exclusion chromatography (SEC-SAXS) and single-particle cryo electron microscopy (cryoEM). Both experimental approaches highlight an unexpected dynamism of the AB-GAPDH system. Moreover, cryoEM reveals that pairs of B-subunits belonging to adjacent tetramers, mutually exchange their CTEs. Protruding like hooks, CTEs dock and penetrate in the active sites of B-subunits of the adjacent tetramer blocking the access of the substrate but leaving vacant the active sites of A-subunits.

2. Materials and methods

2.1. Preparation of AB-GAPDH oligomers

AB-GAPDH enzyme (UniProt code: P19866 and P12860 for A and B subunit, respectively) was prepared from partially purified spinach chloroplasts, following ammonium sulfate precipitation, cold acetone precipitation and anion exchange chromatography, as described in Scagliarini *et al.*, 1998.

Active and inhibited oligomers were obtained incubating overnight at 4°C pure AB-GAPDH enzyme in the presence of 5 m*M* reduced DTT, 1 m*M* $NADP^+$ and 1,3-bisphosphoglycerate (obtained by incubation of phosphoglycerate kinase, 20 U ml^{-1}, with 15 m*M* 3-phosphoglyceric acid, 10 m*M* ATP and 5 m*M* $MgCl_2$) or 5 m*M* oxidized DTT and 1 m*M* NAD^+, respectively. Following incubation, samples were separately loaded into a Superdex 200 10/300 GL (Cytiva) column, pre-equilibrated in 25 m*M* K-phosphate, pH 7.4 plus 0.1 m*M* $NADP^+$, for the active oligomer, or 0.1 m*M* NAD^+, for the inhibited oligomers. Measurements of enzyme activity (Gurrieri *et al.*, 2019) and hydrodynamic radius (see next paragraph), and SDS-PAGE were performed on the fractions of the size exclusion chromatography (SEC) before pooling, changing the buffer and concentrating the samples. Protein concentration was measured by means of the BCA assay and samples were stored at -80°C before the analyses.

2.2. Dynamic light scattering measurements

The hydrodynamic radius (R_h) of AB-samples was measured by Dynamic Light Scattering (DLS) employing a Malvern Nano ZS instrument equipped with a 633 nm laser diode. Samples were introduced in disposable polystyrene cuvettes (100 µl) of 1 cm optical path length. The width of DLS R_h distribution is indicated by the polydispersion index (PdI). In the case of a monomodal distribution (Gaussian) calculated by means of cumulant analysis, $PdI = (\sigma/Z_{avg})^2$, where σ is the width of the distribution and Z_{avg} is the average radius of the protein population. The reported R_h have been averaged from the values obtained from five measurements, each one being composed of ten runs of 10 seconds.

2.3. Small angle X-ray scattering data collection and analysis

In SEC-Small Angle X-ray Scattering (SAXS) experiments, the storage buffer (25 m*M* K-phosphate, pH 7.5) of the active AB-GAPDH sample contained 5 m*M* reduced DTT, 20 m*M* $NADP^+$ and 1,3-bisphosphoglycerate, whereas for the inhibited AB-GAPDH sample the storage buffer contained 0.1 m*M* NAD^+ (Supplementary Table S1A). For SEC elution, 25 m*M* K-phosphate, pH 7.5 buffers with 0.1 m*M* $NADP^+$ or 0.1 m*M* NAD^+ were used for the active and inhibited AB-GAPDH samples, respectively (Supplementary Table S1A). An additional sample of the active form named "active-short", was obtained from the inhibited sample with an incubation time of 2 hours at room temperature in the presence of 5 m*M* reduced DTT, 20 m*M* $NADP^+$ and 1,3-bisphosphoglycerate (Supplementary Table S1A). SEC-SAXS experiments were performed by loading 100-200 µl of samples, onto a Superdex 200 10/300 GL (Cytiva) column connected to the measurement capillary and pre-equilibrated in 25 m*M* K-phosphate buffer (pH 7.5) plus 0.1 m*M* $NADP^+$ or NAD^+ to analyze active or inhibited AB-GAPDH samples, respectively. The SEC separation was run at a flow rate of 0.5 ml min^{-1}. The UV-vis diode array detector of the HPLC system (Shimadzu) recorded the chromatograms at 280 nm before directing the samples to the capillary for SAXS data collection. SAXS frames obtained by 1 s exposure of the

capillary, were acquired continuously. Data collection parameters are reported in Supplementary Table S1B. The automatic pipeline for SEC-SAXS data analysis implemented at BM29 (Pernot *et al.*, 2013) was used to evaluate the quality of the collected data (Brennich *et al.*, 2016) and contributed to the identification of chromatographic regions with constant scattering profiles. Afterwards, a classification of the collected frames as buffer or protein frames was performed on the basis of the SAXS intensity trace; the statistical test implemented in CorrMap (Franke *et al.*, 2015) aided by visual inspection was used to choose the superimposable buffer intensity profiles. The averaging of the buffer scattering data, the subtraction of the averaged buffer intensity from the protein data and an automatic analysis of the subtracted protein profiles were performed with a Matlab script that uses the tools of the ATSAS package (Franke *et al.*, 2017) to automatically evaluate the scattered intensity extrapolated at zero angle I(0) and the radius of gyration (R_g) via the Guinier approximation, and the pair distance distribution function P(r) via the indirect Fourier transform method implemented in GNOM (Svergun, 1992). The frame numbers were converted into retention volumes considering the delay between the injection of the sample into the column and the starting time of the SAXS exposure series. Protein frames giving constant R_g values were scaled to the maximum intensity, checked according to the statistical test (Franke *et al.*, 2015) and then averaged in order to obtain a single representative scattering profile with a better signal to noise ratio. In SAXS experiments performed with the automatic sample changer (SC), the active sample was stored in a 25 m*M* K-phosphate, pH 7.9 buffer containing 1 m*M* $NADP^+$ (Supplementary Table S1C). The 21.2 mg ml^{-1} stock was diluted with the same buffer just before the SAXS measurements to obtain a concentration series in the range 0.1-2.0 mg ml^{-1}, estimated from the dilution factors. The inhibited samples measured as a concentration series in SC mode were directly stored at the final concentration measured by means of BCA assay (0.39-1.89 mg ml^{-1}) or estimated from the dilution factor (0.08-0.2 mg ml^{-1}) in a 25 m*M* K-phosphate, pH 7.5 buffer containing 1 m*M* NAD^+ (Supplementary Table S1C). SC-SAXS measurements on AB-GAPDH samples in active and inhibited conditions were performed by flushing volumes of 50-60 µl and making a set of 10 consecutive exposures during sample flowing in the capillary. The frames were automatically compared to assess the radiation damage and then averaged. The scattering contribution of the capillary filled with buffer was subtracted and the intensity was divided by the protein mass concentration. The absolute intensity scaling using water scattering as a standard (Orthaber *et al.*, 2000) and considering a protein specific volume value of 0.735 cm^3 g^{-1} provided intensities in kDa units. Two repetitions of the measurement procedure for each protein concentration were run and the data were averaged. Sample details and data collection parameters are reported in Supplementary Table S1C, D. Analysis of the scattering profiles was performed with the tools of ATSAS 2.8 (Franke *et al.*, 2017). The I(0) and the R_g were calculated using the Guinier approximation and the indirect Fourier transform method was applied to obtain the P(r) function, with an estimate of the maximum particle dimension (D_{max}), in addition to an independent calculation of I(0) and R_g. The molecular weight was estimated from (i) the Porod volume (V_P) according to the proportionality empirically found for roughly globular proteins (MW ~ 0.625 V_P)

(Petoukhov *et al.*, 2012); (ii) the invariant volume-of-correlation length (V_c) through a power-law relationship between V_c, R_g and MW that has been parametrized (Rambo & Tainer, 2013); and (iii) a method based on an empirical relation to the Porod invariant estimated with a truncated integral (Fischer *et al.*, 2010; Hajizadeh *et al.*, 2018). In addition, the approach based on Bayesian inference to estimate a most probable value and a confidence interval from all these concentration-independent methods was applied (Hajizadeh *et al.*, 2018).

2.4. Theoretical scattering profiles calculation from 3D

Theoretical scattering profiles were calculated from the crystallographic coordinates of oxidized A_2B_2 (PDB ID code 2PKQ) (Fermani *et al.*, 2007) and from the atomic models of AB-GAPDH oligomeric species obtained by the cryoEM analysis (present work), by using CRYSOL 3.0 (Franke *et al.*, 2017) with default parameters and imposing a q range of 0-0.42 $Å^{-1}$ and data points. The theoretical intensities were scaled to have an I(0) coincident with the squared molecular weight of the simulated constructs and employed for the least-square fitting of experimental SAXS profiles as a linear combination of components in which only the volume fractions are optimized, by means of OLIGOMER (Konarev *et al.*, 2003). The optimized volume fractions were converted into protein mass concentration (c; g cm^{-3}) considering the volume fractions equal to mass fractions w_i (assuming all oligomeric species had the same partial specific volume of 0.735 cm^3 g^{-1}) and by multiplying by the overall protein concentration estimated from the I(0) value in absolute units, according to:

$$\boldsymbol{c[g\ cm^{-3}] = \frac{I(0)[cm^{-1}]N_A[mol^{-1}]}{\Delta\rho_M^2\ [cm^2 g^{-2}]\ \ \sum i\ w_i\ MW_i\ [g\ mol^{-1}]}}$$

where N_A is the Avogadro number (6.022 10^{23} mol^{-1}), $\Delta\rho^2_M$ is the squared scattering contrast per mass of protein (5.04 10^{20} cm^2 g^{-2}) and MW_i are the molecular masses of the oligomeric components. An estimate of the contribution of each oligomer in the overall SEC-SAXS elution was obtained by summing up the optimized concentrations of each oligomer for all frames. In order to compare it to the cryoEM particle statistics, this result was also expressed as particle percentage by dividing each overall mass concentration by the MW of each oligomeric component:

$$\%particle_i = \frac{\frac{\sum_{frames} c_i}{MW_i}}{\sum_i \left(\frac{\sum_{frames} c_i}{MW_i}\right)} 100$$

Additional fits of selected SAXS data with the theoretical scattering of single structural components were performed using CRYSOL 3.0 (Franke *et al.*, 2017) in fitting mode (number of spherical harmonics 25, number of fitted data points 51). The fitted q range was selected to 0.01-0.25 $Å^{-1}$ for the SEC-SAXS data and to 0.01-0.30 $Å^{-1}$ for the SC-SAXS data.

2.5. Negative staining EM

Purified inhibited AB-GAPDH oligomers (0.1 mg ml^{-1} AB-GAPDH in 25 m*M* K-phosphate buffer, pH 7.5 and 1 m*M* NAD^+) were first analyzed by negative staining. Briefly a 5 µl drop of sample was applied to a previously plasma cleaned 400 mesh copper carbon film grids and stained with 1 wt/v % uranyl acetate solution. Data were collected on a JEM-1011 (JEOL) transmission electron microscope (TEM), with thermionic source (W filament) and maximum acceleration voltage 100 kV equipped with Gatan Orius SC1000 CCD camera (4008 x 2672 active pixels).

2.6. CryoEM sample preparation and data collection

For cryo-EM grid preparation, a 3 µl droplet of purified inhibited AB-GAPDH sample (1 mg ml^{-1} in 25 m*M* K-phosphate buffer, pH 7.5 and 1 m*M* NAD^+) was plunge frozen in liquid ethane cooled at liquid nitrogen temperature on glow discharged Quantifoil holey TEM grids (Cu, 300 mesh, 1.2/1.3 µm) at 100% humidity and 4.5°C. The grids were blotted with filter paper for 5 s using a Vitrobot Mark IV cryo-plunger (Thermo Fisher Scientific). Grid vitrification optimization was performed on a Tecnai F20 (Thermo Fisher Scientific) Schottky field emission gun transmission electron microscope, equipped with an automated cryo-box and an Ultrascan 2kx2k CCD detector (Gatan). Data collection was performed on a Tecnai F30 Polara cryo electron microscope (Thermo Fisher Scientific, USA) equipped with a Schottky field emission gun operated at 300 kV and using Leginon automated acquisition software (Gatan). A total of 2228 movies were recorded on a K2 Summit direct electron detector (Gatan) in super resolution counting mode at a nominal magnification of 31,000X corresponding to a final pixel size of 1.21 Å (further details are listed in Supplementary Table S2).

2.7. CryoEM image processing

Beam induced motion correction and dose weighting were performed on the collected 2228 movies using MotionCorr2 (Zheng *et al.*, 2017). Contrast transfer function (CTF) correction was performed using CTFFIND4.1 (Rohou & Grigorieff, 2015). Any movies containing low figure of merit scores, substantial drift, low contrast, thick/crystalline ice were manually excluded from further analysis. The majority of data processing steps were conducted in RELION 3.0 (Scheres, 2016; Zivanov *et al.*, 2018). About 1000 representative particles were manually picked from several averaged micrographs. The obtained low pass filtered 2D class averages have then been used for automated particle picking on a total of 1988 averaged micrographs. This resulted in 253954 particles which were extracted and down-sampled (64 X 64) for several iterative rounds of 2D classification and selection. A total of 127963 particles from 2D classes that possessed the quaternary features of the different GAPDH oligomers were subjected to unsupervised 3D classifications (number of classes K=8) using two unbiased low resolution initial models (an ellipsoid and a sphere). Each 3D classification resulted in eight 3D classes of which two had the quaternary structures corresponding to $A_{10}B_{10}$ and A_8B_8 (classes 7 and 8,

Supplementary Fig. S1A top) and to A_4B_4 and A_8B_8 (classes 3 and 6, Supplementary Fig. S1A bottom), respectively. New analyses were then run separately for each oligomer, including the dissociated A_2B_2. This species, although not resulting in the first overall 3D classification, was clearly observed in negative staining and cryoEM micrographs (Supplementary Figs. S2A, B) and in the overall 2D classification. For each oligomer an automated particle picking round was repeated with Gautomatch (https://www.mrc-lmb.cam.ac.uk/kzhang/) using as template the low pass filtered 2D projections derived from the corresponding cryoEM electron density maps obtained in the previous 3D classification. After several rounds of 2D classification and selection, a total of 48558, 31023, 64130 and 33067 particles for A_2B_2, A_4B_4, A_8B_8 and $A_{10}B_{10}$, respectively were subjected to a new 3D classification using as initial models their correspondent low pass filtered (40 Å) previously obtained cryoEM electron density maps (Supplementary Fig. S1B). The initial model for the dissociated A_2B_2 tetramers was instead calculated from its assigned 2D averages using the initial model generation tool within RELION3.0 (Scheres, 2016; Zivanov *et al.*, 2018). After 3D classifications 19636 particles were assigned to the dissociated A_2B_2 (K=4), 20777 particles were assigned to A_4B_4 (K=4), 34379 to A_8B_8 (23611 particles to the main form and 10768 particles to its alternative conformer, K=8) and finally 7352 particles were assigned to $A_{10}B_{10}$ (K=4). These subsets of particles, after being re-extracted at full resolution, were used for the final refinement. We obtained symmetry-constrained maps at 6.7 Å (D2 point group symmetry), 8.9 Å (C1 point group symmetry), 5.7 Å (C2 point group symmetry), 7.1 Å (C2 point group symmetry) and 13 Å (C5 point group symmetry) for A_2B_2, A_4B_4, A_8B_8 (both main and alternative conformer) and $A_{10}B_{10}$ oligomers, respectively. Identical maps were obtained for A_4B_4, and both A_8B_8 conformers, by removing symmetry constraints (i.e. imposing the C1 symmetry) during the refinement with RELION 3.0 (Scheres, 2016; Zivanov *et al.*, 2018). The resolution of the final maps was estimated by the 0.143 FSC criterion after a post-processing procedure. Estimation of the local resolution was done in ResMap (Kucukelbir *et al.*, 2014). Handedness of the reconstructions was determined by fitting the GAPDH oligomeric models (see below) into the obtained maps using the 'fit in map' tool in Chimera 1.15 (Pettersen *et al.*, 2004).

2.8. Modelling and bioinformatics tools

The GAPDH oligomeric models were obtained first by placing and manually fitting in their corresponding final cryoEM density map, the crystallographic oxidized A_2B_2 model (PDB ID 2PKQ) (Fermani *et al.*, 2007) and then by rigid-body fitting using the 'fit in map' tool in Chimera (Pettersen *et al.*, 2004). The CTEs of the B-subunits belonging to the more resolved GAPDH oligomers cryoEM density maps (i.e. the A_4B_4 and A_8B_8) were built as C_α backbones using COOT (Emsley *et al.*, 2010). Afterward, the obtained GAPDH models were independently refined into their corresponding cryoEM density maps using iterative cycles of Phenix real space refinement (Afonine *et al.*, 2018) and COOT (Emsley *et al.*, 2010) manual adjustment. Cross correlation analyses, measures of distances, areas and

angles, 3D visualizations and rendering were performed using Chimera (Pettersen *et al.*, 2004) and ChimeraX (Pettersen *et al.*, 2021). GAPDH oligomers protein interfaces, contacts and free energy of assembly dissociation were calculated using PDBePISA (Krissinel & Henrick, 2007) and visualized using Chimera (Pettersen *et al.*, 2004).

2.9. Data availability

The cryoEM maps of AB-GAPDH oligomers and the coordinates of atomic models generated and analyzed in the current study, have been deposited in the Electron Microscopy Data Bank and in the Protein Data Bank, under accession codes: EMD-13824 and PDB ID 7Q53 for A_2B_2; EMD-13825 and PDB ID 7Q54 for A_4B_4; EMD-13826 and PDB ID 7Q55 for A_8B_8 (main conformer); EMD-13827 and PDB ID 7Q56 for A_8B_8 (alternative conformer), EMD-13828 and PDB ID 7Q57 for $A_{10}B_{10}$.

3. Results and Discussion

3.1. Fingerprinting multiple oligomeric states of AB-GAPDH with SEC-SAXS

The SEC-SAXS data were collected on active and inhibited (i.e. $NADP^+$- and NAD^+-bound, respectively) AB-GAPDH oligomers. The quaternary structure of samples was previously checked by DLS. Average hydrodynamic radius (R_h) values of 52 and 100 Å corresponding to apparent molecular weight (MW) of 159 and 736 kDa, were obtained for active and inhibited samples, respectively. As a reference, the theoretical MW of A_2B_2-GAPDH tetramers is 150 kDa. An additional sample named "active-short" obtained incubating the inhibited sample under activating conditions for a shorter incubation time (2 hours instead than overnight), was measured by SEC-SAXS. SAXS experiments showed that all samples presented a systematic variation of dimensional parameters, underlying the presence of different oligomers in addition to the more abundant A_2B_2 and A_8B_8 species expected in active and inhibited samples, respectively (Fig. 1A and Supplementary Fig. S3) (Fermani *et al.*, 2007; Scagliarini *et al.*, 1998; Scheibe *et al.*, 1996; Sparla *et al.*, 2002). Statistically superimposable frames showing a constant gyration radius (R_g) were identified and averaged to obtain representative SAXS profiles (Fig. 1A and Supplementary Table S3) interpretable as AB-GAPDH oligomers on the basis of their dimensional parameters and distance distribution functions (P(r)) (Fig. 1 and Supplementary Fig. S3 and Table S4). In the inhibited sample, the predominant species (maximum elution volume at 13 ml) showed a R_g of 67 Å, a maximum size (D_{max}) of 200 Å and a MW between 500 and 600 kDa, compatible with the expected A_8B_8 oligomer (Supplementary Table S3). In addition, a larger species (eluted around 12 ml) was identified, with a R_g around 80 Å, a D_{max} of 280 Å and an estimated MW between 650 and 700 kDa, suggesting an $A_{10}B_{10}$ stoichiometry. A less abundant and smaller component was also observed at larger elution volumes (around 15 ml) (Fig. 1A, pink symbols). The estimation of its R_g and MW was more uncertain. The related P(r) profile showed a D_{max} around 150 Å and only one maximum around 50 Å, clearly distinguishable from the bimodal P(r) function of A_8B_8 (Fig. 1B). A similar P(r)

profile (Fig. 1C) was calculated at the beginning of the elution of the active-short sample (around 13.5 ml) again indicating the presence of a wide range of estimated MWs (Fig. 1A inset, purple diamonds). At the elution maximum of the active-short sample (14.8 ml), the detection of distinct SEC peaks appeared not possible (Stevens, 1989). The corresponding R_g and D_{max} values (40 Å and 140 Å, respectively) suggest the co-existence of A_2B_2 and higher order oligomers in a fast-exchange equilibrium possibly involving A_4B_4 as an intermediate species (Fig. 1A, red symbols, Supplementary Fig. S3 and Table S4). The presence in vivo of the A_4B_4 was already reported in different plant species (Baalmann *et al.*, 1994; Howard *et al.*, 2008, 2011) besides the common A_2B_2 and A_8B_8-GAPDH forms, supporting the idea that this oligomer is not only an intermediate in the aggregation of A_2B_2 to A_8B_8, but even an essential player for AB-GAPDH regulation. The dimensional parameters of the active-short sample decreased gradually towards larger retention volumes and at the end of the elution (around 16.4 ml), the structural parameters agreed with those found at the elution maximum of the active sample (15.4 ml), i.e. a R_g of 34 Å and a D_{max} around 100 Å, compatible with an A_2B_2 tetramer (Fig. 1D).

3.2. Single-particle cryoEM analysis confirms the heterogeneity of inhibited AB-GAPDH

In agreement with SAXS results, in inhibiting conditions the single-particle analysis revealed the coexistence of different oligomeric states of the enzyme (Fig. 2). Projections related to different GAPDH oligomers, namely A_2B_2, A_4B_4, A_8B_8 and $A_{10}B_{10}$, were clearly present in negative stain and cryoEM micrographs (Supplementary Fig. S2). They were also present in the 2D and 3D classifications performed on the complete GAPDH data set (Fig. 2A and Supplementary Fig. S1A). An estimation of the relative abundance of each oligomer obtained from the number of refined particles, showed that the A_8B_8 hexadecamer is the most abundant species (42%), albeit in two distinct conformers, named main (29%) and alternative (13%) (Fig. 2B). The A_4B_4 octamer (25%) and the A_2B_2 tetramer (24%) are less abundant. The remaining 9% corresponds to the $A_{10}B_{10}$ icosamer. The cryoEM density map of the A_2B_2 tetramer was determined at 6.3 Å (Fig. 2B and Supplementary Fig.S4). Superimposing the A_2B_2 cryoEM map to the crystal structure of oxidized A_2B_2-GAPDH complexed with $NADP^+$ (PDB ID 2PKQ) (Fermani *et al.*, 2007) no significant conformational differences are observed. The 8.9 Å A_4B_4 cryoEM density map is an octamer with C1 symmetry formed by two A_2B_2 tetramers rotated each other by approximately 180° (Figs. 2B and 3A and Supplementary Fig. S5A, B). Imposition of C2 symmetry in the 3D refinement process produced a less resolved reconstruction, due to inherent conformational differences between the two A_2B_2 tetramers. The A_8B_8 hexadecamer was found in two conformations, both with C2 symmetry and formed by two A_4B_4 dimers. The 5.7 Å cryoEM density map of the main conformer shows a central cavity with an area of 1763 $Å^2$ (Figs. 2B and 3D-I and Supplementary Fig. S5C, D). Compared to the main conformer, the two A_4B_4 dimers of the alternative conformer are lightly shifted in the x direction, one in respect to the other, and the central cavity has a similar area (1738 $Å^2$) (Fig. 2B and Supplementary Fig. S6).

Finally, the 13 Å $A_{10}B_{10}$ electron density map is a pentamer of A_2B_2 tetramers with C5 symmetry and a central 5531 $Å^2$ wide seastar-shaped cavity (Fig. 2B and Supplementary Fig. S7). In all oligomers, the contacts between A_2B_2 tetramers are mediated by B-subunits as shown by rigidly fitting the oxidized A_2B_2 crystal structure (PDB ID 2PKQ) (Fermani *et al.*, 2007) inside their respective cryoEM density maps (Figs. 2B, 3A, B and E-H, and Supplementary Figs. S6A-C and S7A-C). Although A- and B-subunits show a high sequence identity (~81%; Supplementary Fig. S8) and similar overall structure, the positioning of B-subunit rather than A-subunit at the contact regions between adjacent tetramers, gave higher correlation coefficients (Supplementary Table S5). Consistently, it is long known that AB-GAPDH aggregation depends on the CTE of the B-subunits (Sparla *et al.*, 2005, 2002).

3.3. Dissecting the assembling of A_2B_2-GAPDH tetramers in higher order oligomers: the role of the CTE

The cryoEM density maps of A_4B_4 and both conformers of A_8B_8 showed in proximity of the contact regions between adjacent A_2B_2 tetramers, additional densities with respect to the density of the GAPDH core protein, (Fig. 3 and Supplementary Fig. S6A-C). These densities start from the last B-subunit residue of the fitted A_2B_2 crystal structure and continue in the catalytic domain of the closest B-subunit of the adjacent tetramer about 20 Å far away. In some cases the density was clearly visible and continuous, in others was less defined. A model of the C_α backbone of the CTE, including the side chains of Cys349 and Cys358 forming the regulatory disulfide bridge, was built on the basis of the electron density map of the A_8B_8-GAPDH main conformer. The model consists of an extended linker region visible in the electron density maps at lower density threshold, followed by a helix, a circular motif determined by the disulfide bond and a final random coil region (Figs. 3B, F, H and 4A). In all GAPDH oligomers the CTEs mediate the connection between B-subunits belonging to adjacent A_2B_2 tetramers, and each tetramer is connected with the adjacent one by two CTEs. The CTE belonging to one B-subunit penetrates into the catalytic domain of the B-subunit of the adjacent tetramer whose CTE in turn enters into the catalytic domain of the B-subunit of the first tetramer in the opposite direction (Figs. 3A, B and D-H and Supplementary Figs. S6B and C). The catalytic sites of the A-subunits, two per tetramer, remain free. The CTE linker regions (Figs. 3B, F, H and Supplementary Fig. S6C) differ significantly from each other in length (from 15 Å to 22 Å) and conformation among and inside the different oligomers. This observation justifies the symmetry shown by A_4B_4 and A_8B_8 oligomers (C1 and C2, respectively), lower than the expected from stoichiometry. The CTE linker regions are indeed highly flexible as indicated by the significant decrease in resolution in the CTE linker regions (Fig. 3C, I and Supplementary Fig. S6D). The A_2B_2 and A_4B_4 oligomers have two "non-engaged" CTEs each one, since there are not adjacent tetramers in which the free CTEs can slip into the B-subunit catalytic site. These "non-engaged" CTEs are likely free to move in the surroundings assuming various conformation and positions and for this reason their corresponding electron density is not observed (Fig. 3A and Supplementary Fig. S4A). These "non-engaged" CTEs make A_2B_2 and A_4B_4 able to form higher

oligomers. Consistently, the chimeric form composed of A-subunits fused with CTE [$(A+CTE)_4$] has four "non-engaged" CTEs and makes oligomers that reach an unexpectedly high molecular mass, at least 7-fold bigger than the corresponding tetramer (Sparla *et al.*, 2005, 2002). Considering that the A_8B_8 oligomer shows each CTE engaged with another B-subunit (Figs. 3D-H and Supplementary Fig. S6A-C), it can be the end-point of the oligomerization process. A similar situation is probably present in the $A_{10}B_{10}$, but the limited resolution of the electron density map prevented the CTE reconstruction (Supplementary Fig. S7A-D). The last portion of the CTE (helix, circular motif and terminal random coil) of each B-subunit penetrates into the catalytic site of a B-subunit of the adjacent tetramer through the large cavity formed between the bound cofactor NAD(H) and the S-loop (Fig. 4A), ending in the Ps site that hosts the phosphate groups of the substrate (1,3-bisphosphoglycerate) and very close to the hydroxyl groups of the nicotinamide ribose (Fig. 4B). Therefore, the CTE prevents the access and binding of the substrate in the B-subunit active site. Moreover, a reversible oxidation of the catalytic cysteine 149 (sulphenic form) can be envisaged in the inactivating conditions, differently to what is reported in Zaffagnini *et al.*, 2019 and Lia *et al.*, 2020 for cytosolic *Arabidopsis thaliana* and human GAPDH, respectively.

Arginines 195 and 231 of the B-subunit involved in the stabilization of the Ps site (Fermani *et al.*, 2007) are likely to interact with the terminal Glu362 (Supplementary Fig. S8). Further positive residues of the B-subunit S-loop, such as Arg183 and His190, could contribute to set in place the negatively charged CTE. Moreover, the various negatively charged and bulky residues of the CTE (e.g. Asp355, Glu356 and Glu357; Supplementary Fig. S8) could possibly interfere with the correct positioning of the $NADP^+$ 2'-phosphate group. This hypothesis explains why the enzyme needs to replace NADP(H) with NAD(H) in order to assemble in oligomers and why the phosphate cofactor promotes oligomer dissociation. The cavity occupied by the CTE in A_8B_8 cryoEM structure is the same observed in the crystal structure of oxidized A_2B_2 complexed with $NADP^+$ (PDB ID 2PKQ) (Fermani *et al.*, 2007). In this last structure, it was possible to build only less than ten C-terminal residues of the two CTEs belonging to the B-subunits of the tetramer. Nevertheless, the superimposition of the two structures shows that the last portion of CTE has a different conformation and in oxidized A_2B_2-GAPDH complexed with $NADP^+$ ends in the more external region of the catalytic cavity leaving free the Ps and the Pi sites (Fig. 4C) (Fermani *et al.*, 2007; Matsumura et al., 2011). The CTE responsible of all regulatory properties of A_2B_2-GAPDH, is considered evolutionarily derived from CP12, being homologous to the C-terminal domain of CP12 (Baalmann *et al.*, 1996; Sparla *et al.*, 2002). The structural models of the binary A_4-GAPDH/CP12 and ternary A_4-GAPDH/CP12/PRK complexes (Fermani *et al.*, 2012; Matsumura *et al.*, 2011; McFarlane *et al.*, 2019; Yu *et al.*, 2020) reveal that the CTE in A_8B_8-GAPDH and the C-terminal domain of CP12 share not only the same cavity but also a very similar conformation, especially the α-helix portion (Fig. 4D). The unique striking difference is that CP12 penetrates more deeply in the GAPDH active site compared to CTE, blocking both Ps and

the Pi sites. Indeed, the side chain of Asn78, the last CP12 residue, has been observed at an H-bond distance from the thiol group of the catalytic Cys149 (Fermani *et al.*, 2012; Matsumura *et al.*, 2011; Yu *et al.*, 2020).

3.4. Interface analysis of AB-oligomers

The A_2B_2 tetramers within oligomers are linked together by the CTEs but appear to interact also through a different surface. PDBePISA (Krissinel & Henrick, 2007) calculations showed that in all GAPDH oligomers the CTEs contribute to the interface area between A_2B_2 tetramers by 39% in A_4B_4, 32% and 33% in A_8B_8 and its alternative conformer, respectively (SI Appendix, Table S4). The A_8B_8 oligomer shows the largest total interface area (2641 $Å^2$) and consequently the largest average single interface area equal to 660 $Å^2$ (449 $Å^2$ without CTE). This area decreases to 625 $Å^2$ (421 $Å^2$ without CTE) in the case of the alternative conformer and to 656 $Å^2$ (403 $Å^2$ without CTE) for A_4B_4. The $A_{10}B_{10}$ has the smallest average single interface area (228 $Å^2$). CTE-independent interacting surfaces are similar in all oligomers and invariably include four stretches of residues (77-80; 97-114; 119-127; 139-143) located in α-helices and loops (Fig. 3, Supplementary Figs. S6C and S8). The last two stretches contain two amino acid insertions in B- compared to A-subunit (Ser123A and Val140) and various sequence differences (Supplementary Fig. S8). This may explain (Hashimoto & Panchenko, 2010) why artificial tetramers made of B-subunits only (B_4) or $(A+CTE)_4$ form oligomers of different size under inhibiting conditions (491 vs >1800 kDa, respectively) (Baalmann *et al.*, 1996; Sparla *et al.*, 2002, 2005). In A_4B_4 and A_8B_8 oligomers, but not in $A_{10}B_{10}$, additional interface regions comprise residues from the S-loop (179-195) and residues between strands β2 and β3 (206-208 and 215-222). Intriguingly, the CTEs also play a key role in improving the thermodynamic stability of both A_4B_4 and A_8B_8 oligomers. The calculated dissociation free energy (ΔG_{diss}) is negative in all oligomers without CTEs indicating that they are unstable, while the presence of CTE prevents their dissociation (Supplementary Table S6). The most stable oligomer is A_8B_8 in the main conformation (ΔG_{diss} = 41 kcal mol^{-1}), followed by A_4B_4 (ΔG_{diss} = 35.9 kcal mol^{-1}) and the hexadecamer alternative conformer (ΔG_{diss} = 35.5 kcal mol^{-1}).

3.5. SEC-SAXS data matching with AB-structural models

The theoretical scattering profiles of cryoEM models of the AB-GAPDH oligomers (here presented), and the A_2B_2 crystal structure (PDB ID 2PKQ) (Fermani *et al.*, 2007) were calculated (Supplementary Fig. S9) to evaluate the agreement with SEC-SAXS data and the contribution of the different oligomers. The inhibited sample relative abundance (particles percentage of 19%, 49%, 30% and 2% for $A_{10}B_{10}$, A_8B_8, A_4B_4 and A_2B_2, respectively) shows a general agreement with the cryoEM data, except for the negligible contribution of A_2B_2 and a larger fraction of $A_{10}B_{10}$ (Fig. 2B; Supplementary Fig. S10A, D). The comparison between the theoretical and experimental scattering profiles suggests that the data from the inhibited sample can be also interpreted reasonably well in terms of one prevailing oligomer at their

elution maxima i.e. $A_{10}B_{10}$, A_8B_8 and A_4B_4 (Supplementary Fig. S10E; grey vs. black line). The A_4B_4 coexists with the predominant A_8B_8 in an exchange process and its scattering became dominant only at the tail of the elution (Supplementary Fig. S10A). Data from the active sample are well interpreted by the scattering profile of the A_2B_2 tetramer (Supplementary Fig. S10C, D and G and Table S7), while the active-short sample consists of a more complex mixture, predominantly composed by the A_2B_2 form coexisting with a significant fraction of A_4B_4 oligomer and AB dimers (Supplementary Fig. S10B, F). The introduction of this last form, already described for non-photosynthetic GAPDHs (Roitel *et al.*, 2003; Torres-Bugeau *et al.*, 2012), clearly improved the fitting (Supplementary Fig. S10F; black vs. grey line). However, the absence in the experimental data of the pronounced minimum observed at q=0.1 $Å^{-1}$ in the A_2B_2 theoretical scattering profile, can also be ascribed to a quaternary structure rearrangement in solution, that generates a less compact and isometric tetramer (Del Giudice *et al.*, 2015; Ferreira-da-Silva *et al.*, 2006). Concentration effect on the oligomerization of AB-GAPDH SAXS measurements without SEC separation (SC-SAXS) on AB-GAPDH in inhibited and active conditions were also performed (Supplementary Table S8). The inhibited sample can be described as a mixture in which the $A_{10}B_{10}$ oligomer is predominant (roughly 50% volume fraction), coexisting with the A_8B_8 oligomer (35%) and a smaller fraction of the A_4B_4 form (15%) (Supplementary Fig. S11A, B and C). In the active sample, a systematic decrease of the average dimensions and forward scattered intensity was observed with the decrease of the protein concentration (Supplementary Table S8). The P(r) functions underwent a systematic decrease of the additional peak at 100 Å seen in the bimodal P(r) of higher oligomers, in favour of the main peak at 50 Å characteristic of the A_2B_2 tetramer (Supplementary Fig. S11D). The data fitting in terms of a mixture suggests that the fraction of A_2B_2 increased from roughly 20% to above 60% upon dilution, at the expenses of the A_4B_4 and $A_{10}B_{10}$ oligomers, present as 50% and 27% volume fractions, respectively, in the most concentrated sample (Supplementary Fig. S11E, F and Table S9). This analysis shows that the cryoEM models explain a consistent amount of the SAXS signal. However, the AB-GAPDH oligomerization equilibrium in solution appears more complex. Indeed, partially formed oligomers or less symmetric conformations of $(A_2B_2)_n$ (n=4 and 5) oligomers such as polymeric chains of A_2B_2 units with free CTEs, and small fractions of larger assemblies (n>5), could explain the non-optimal agreement of the fits based on the cryoEM models only and the maximum sizes larger than 240 Å (expected for the $A_{10}B_{10}$ oligomer) detected in the inhibited sample.

3.6. Concluding remarks

NAD(P)H-dependent GAPDH enzymes are involved in photosynthetic carbon assimilation of all oxygenic phototrophs. However, whereas cyanobacteria and most eukaryotic algae exclusively present a homotetrameric form (A_4-GAPDH), the major chloroplast GAPDH isozyme of land plants is formed by A and B subunits, the latter containing a redox-sensitive C-terminal extension (CTE) which controls

the NADPH-dependent activity of the enzyme and the capability to form higher order oligomers (Baalmann *et al.*, 1996; Sparla *et al.*, 2002).

In this study, we have structurally characterized photosynthetic AB-GAPDH and disclosed the CTE-mediated regulation/oligomerization process, by combining SEC-SAXS and single-particle cryoEM analysis. Both experimental approaches highlighted the presence in both active and inhibited in vitro conditions (mimicking light and dark in vivo conditions) of various oligomers in addition to the expected species with A_2B_2 and A_8B_8 stoichiometries, respectively (Fermani *et al.*, 2007; Scagliarini *et al.*, 1998; Scheibe *et al.*, 1996; Sparla *et al.*, 2002). In activating conditions beside the heterotetramer A_2B_2, the octamer A_4B_4 was detected, while in inhibiting conditions the population increases to four species, i.e. $(A_2B_2)_n$ with n=1, 2, 4 and 5 (Figs. 1 and 2). The unexpected heterogeneity of the AB-GAPDH system is not simply ascribable to the experimental conditions. Indeed, A_4B_4 oligomers were observed in leaves of different plant species (Howard *et al.*, 2008, 2011), indicating that this form is both an intermediate step in GAPDH oligomerization and an essential player in its regulation. Moreover, being A_4B_4 a structural unit of A_8B_8 and likely of $A_{10}B_{10}$ oligomers, it represents for the AB-GAPDH system a ubiquitous reservoir of inhibited A_2B_2 tetramers that when needed can easily dissociate to form the active species or aggregate in higher molecular weight oligomers. In all oligomers, the interfaces between A_2B_2-tetramers uniquely involve B-subunits (Figs. 2B and 3), confirming that the CTE manages the AB-GAPDH assembly process upon NADP(H)/NAD(H) cofactor exchange. Moreover, the higher resolution A_4B_4 and A_8B_8 cryoEM models show that pair of B-subunits from adjacent tetramers hug each other through their CTEs (Figs 3A, B, E-H and Supplementary Fig. S6B, C). Each CTE slips into the cofactor cavity of the partner B-subunit up to its catalytic Ps site, effectively preventing the substrate binding (Fig. 4). This positioning of the CTE is only possible if NAD(H) is bound to the A-subunit. However, NAD(H) does not promote oligomerization directly, but it does so by replacing NADP(H). Indeed, the 2'-phosphate of NADP(H) is apparently incompatible with the allocation of the CTE in the active site of B-subunits, justifying the disassembling role of this cofactor (Sparla *et al.*, 2002). On the other hand, the catalytic sites of A-subunits are free and likely available to perform the constitutive NADH-dependent catalysis.

The conformation assumed by the last portion of the CTE closely resembles that one of the CP12 C-terminal domain in the GAPDH-CP12-PRK ternary complex (PDB ID 6GVE) (McFarlane *et al.*, 2019) (Fig. 4C), indicating that the molecular strategy for the modulation of GAPDH activity appears conserved among all photosynthetic GAPDHs.

In conclusion, our structural study provides a full picture at molecular level showing how the dynamic changes in the oligomeric status of AB-GAPDH contribute to the modulation of the Calvin-Benson cycle in response to light conditions occurring in the natural environment.

1

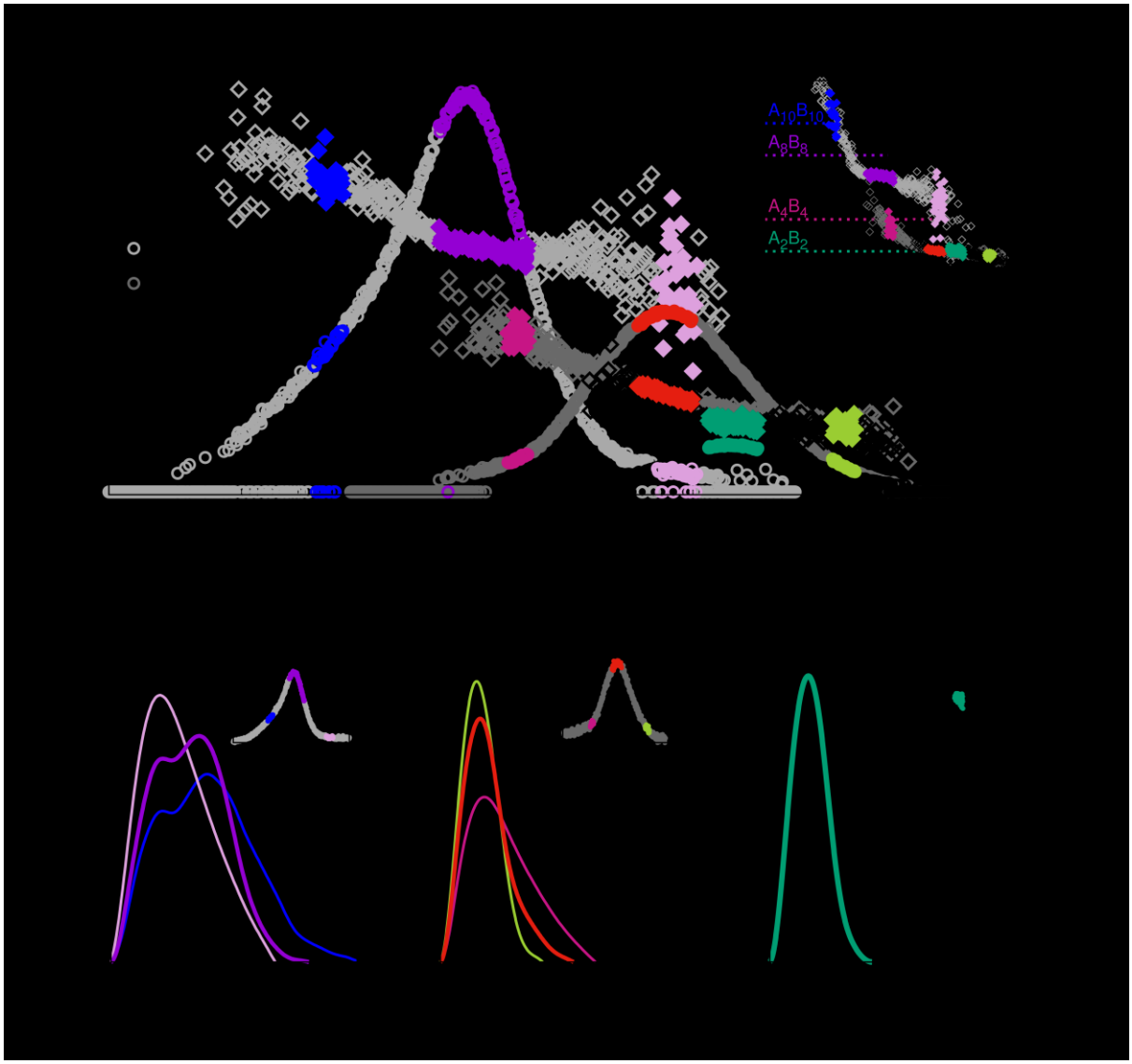

Figure 1 (A) Parameters derived from the analysis of SAXS frames for the three AB-GAPDH samples: inhibited (light grey symbols, maximum at 13 ml), active-short (grey symbols, maximum at 14.8 ml) and active (black symbols, maximum at 15.4 ml), are shown as a function of the SEC elution volume. The data points belonging to the frames averaged to obtain the selected scattering profiles are highlighted with a colour code. The elution profile given by the scattering intensity at zero angle (I(0), circles, right ordinate axis) is plotted together with the radius of gyration (R_g) obtained from the Guinier approximation (diamonds, left ordinate axis). In the inset, molecular weight (MW) estimated from the Porod volume (MW(V_P), diamonds). The MWs expected on the basis of the protein sequence for $(A_2B_2)_n$ oligomers with n=1, 2, 4 and 5 are reported as dashed lines for reference. P(r) functions calculated from the selected scattering profiles in the elution of the samples: (B) inhibited, (C) active-short, (D) active; in the insets the elution profiles given by the SAXS integrated intensity are also shown.

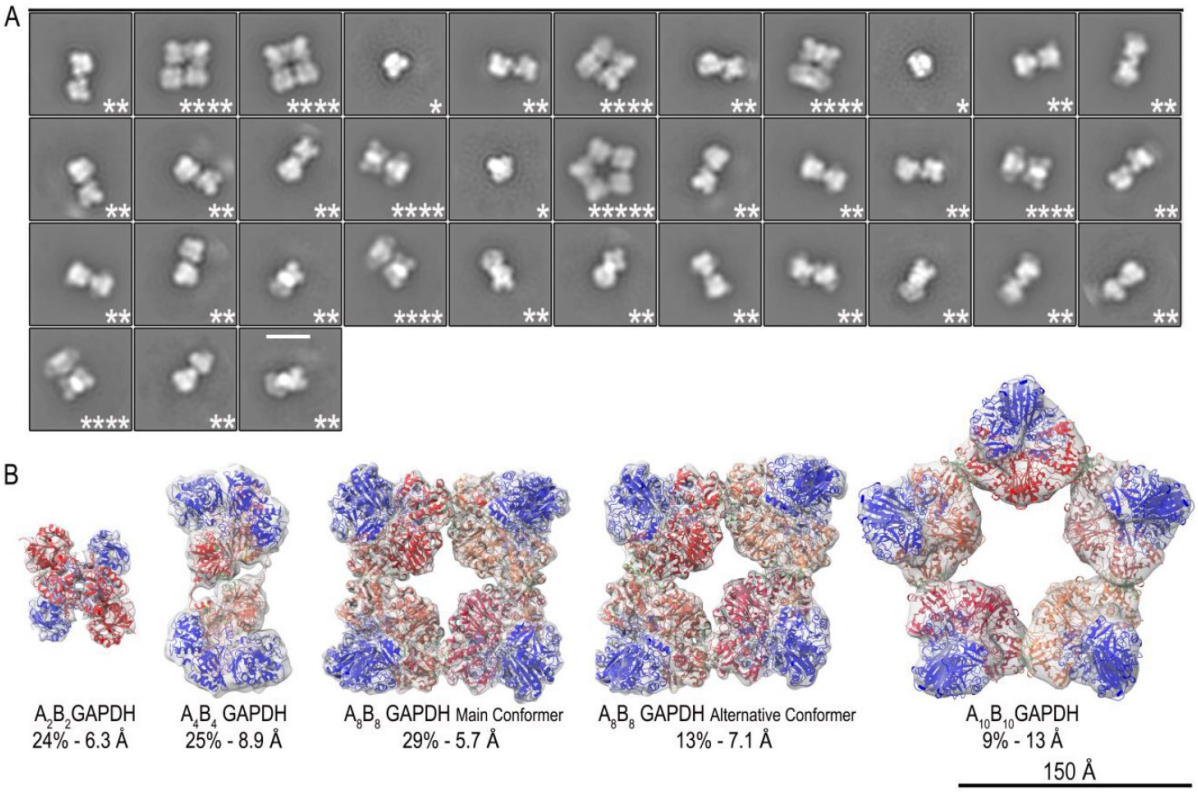

Figure 2 (A) Representative single-particle 2D classification obtained from the complete GAPDH data set showing the presence of class averages attributable to A_2B_2, A_4B_4, A_8B_8 and $A_{10}B_{10}$ oligomers. For each species, the number of A_2B_2 tetramers is indicated by asterisks. The scale bar is 150 Å. (B) GAPDH oligomer cryoEM density maps fitted with models derived from the crystal structure of the oxidized A_2B_2 complexed with $NADP^+$ (PDB ID code 2PKQ) (Fermani *et al.*, 2007). The O/Q, A/C, E/G, K/I and M/S B-subunits are represented in red, tomato, crimson, coral and indian red, respectively. The A-subunits are in blue. The numbers below the cryoEM electron density maps represent the oligomer relative abundances and their resolutions, respectively.

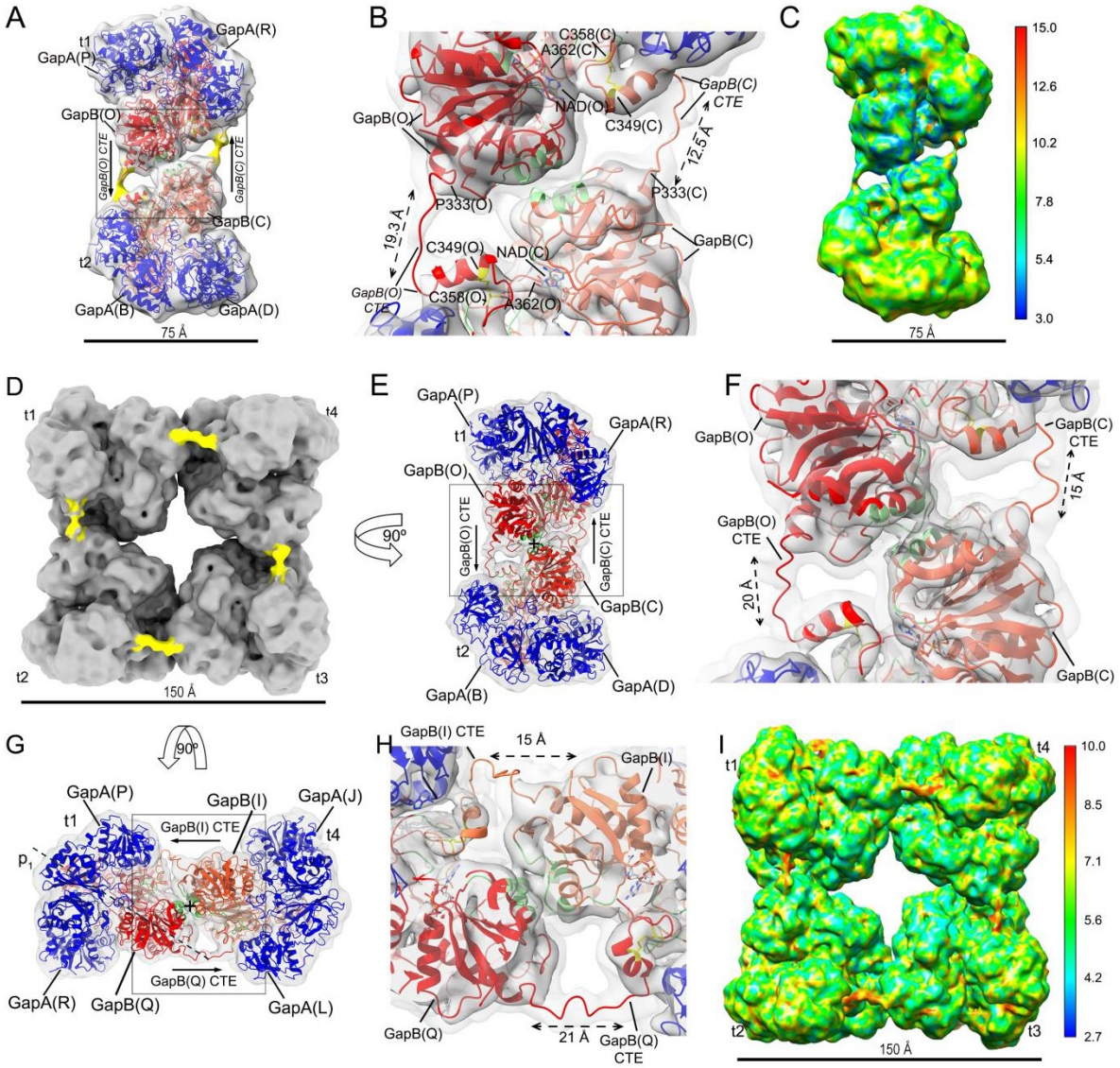

Figure 3 (A) CryoEM density map of the A_4B_4 oligomer at 8.9 Å resolution. The map, shown at low density threshold, reveals two regions (highlighted in yellow) connecting the t1 and t2 A_2B_2 tetramers. (B) Detail of the region boxed in (A). (C) CryoEM electron density map of the A_4B_4 oligomer filtered according to ResMap local resolution. (D) CryoEM electron density map of the A_8B_8 oligomer shown at a low density threshold. Note the connecting regions (highlighted in yellow) among the GAPDH tetramers t1-t4. (E) Side view of the maps in (D) showing the t1 and t2 tetramers. (F) Detail of the boxed region in (E). (G) Side view of the map in (D) showing the t1 and t4 tetramers. (H) Detail of the region boxed in (G). (I) CryoEM electron density map of the A_8B_8 oligomer filtered according to ResMap local resolution. All maps are fitted with their corresponding model derived from the crystal structure of the oxidized A_2B_2 complexed with $NADP^+$ (PDB ID code 2PKQ) (Fermani *et al.*, 2007). The O/Q, A/C, E/G, K/I and M/S B-subunits are represented in red, tomato, crimson, coral and indian red, respectively. The A-subunits are in blue. In (B), (F) and (H), the densities of the 3D reconstructions are displayed at

two different isosurface levels (higher in dark gray and lower in light gray) and the interfacing residues between adjacent GAPDH tetramers are highlighted in green.

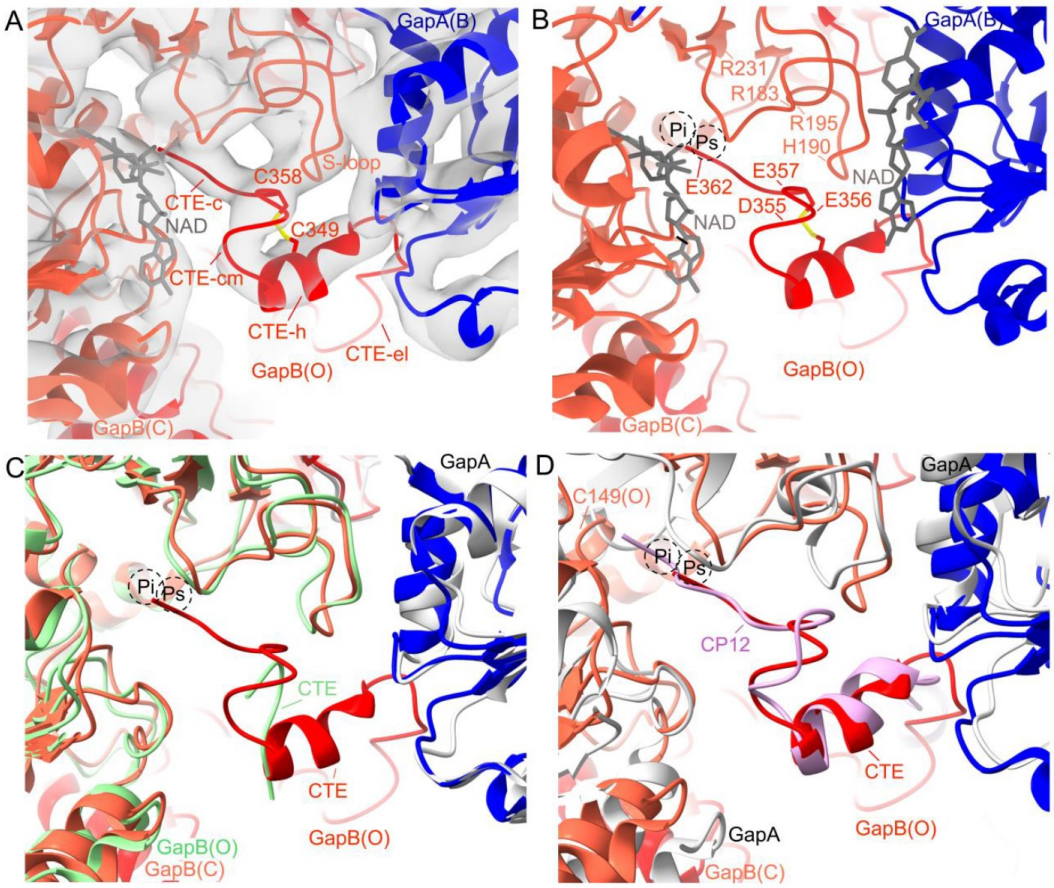

Figure 4 (A) Detail of the CTE of B-subunit (chain O) in red inserted in the active site of B-subunit (chain C) in tomato, of the adjacent A_2B_2 tetramer. The A-subunit (chain B) is in blue. CTE-el: CTE extended linker; CTE-h: CTE helix; CTE-cm: CTE circular motif; CTE-c: CTE random coil. (B) Detail of the CTE of B-subunit (chain O) in red inserted in the active site of B-subunit (chain C) in tomato, of the adjacent A_2B_2 tetramer. The A-subunit (chain B) is in blue. The negatively charged residues of CTE likely interacting with the positively charged residues of B-subunit are indicated. The NAD^+ bound to the A-subunit is also shown. The Ps and Pi labels indicate the substrate binding site. (C) Detail of the CTE of B-subunit (chain O) in red superimposed to the CTE of B-subunit (chain O) in green from the crystal structure of the oxidized A_2B_2 complexed with $NADP^+$ (PDB ID code 2PKQ) (Fermani *et al.*, 2007). The B-subunit (chain O) and the A-subunit of A_2B_2 crystal structure are in green and light grey, respectively. Colour code for cryoEM structure is as in panels (A) and (B) Note that the two CTEs shows a different conformation and the CTE from A_2B_2 crystal structure ends in the more external region of the catalytic cavity, far away the substrate binding site (Ps and Pi sites). (D) Detail of the CTE of B-subunit (chain O) in red superimposed to the CP12 C-terminal domain in violet, from the cryoEM model of the ternary GAPDH-CP12-PRK complex (PDB ID 6GVE) (McFarlane *et al.*, 2019). The A-subunits of GAPDH from the complex crystal structure are shown in light grey. The catalytic Cys149

is indicated. Note that CTE and the C-ter domain of CP12 have a very similar conformation and CP12 fills both the Ps and the Pi sites differently from CTE which ends in the Ps.

Acknowledgements We deeply thank Prof. Viorel Nicolae Pavel for his essential suggestions on SAXS experiments and data analysis. This work has been supported by Instruct, project number PID 1829 “Unravelling the pathway of regulation of photosynthetic AB-GAPDH by cryo-EM” funded by the Horizon 2020 programme of the European Union. The high-resolution data were collected at the IBS - Institut de Biologie Structurale in Grenoble (France) with assistance from Dr. Guy Schoehn. We thank the European Synchrotron Radiation Facility for allocation of SAXS beam time (BAG Proposals MX1750) and the staff of beamline BM29 for technical support. S.F. and G.F. thanks the Consorzio Interuniversitario di Ricerca in Chimica dei Metalli nei Sistemi Biologici (CIRCMSB).

References

Afonine, P. V., Poon, B. K., Read, R. J., Sobolev, O. V., Terwilliger, T. C., Urzhumtsev, A. & Adams, P. D. (2018). Acta Crystallogr. D Struct. Biol. **74**, 531-544.

Baalmann, E., Backhausen, J. E., Kitzmann, C. & Scheibe, R. (1994). Botanica Acta. **107**, 313-320.

Baalmann, E., Backhausen, J.E., Rak, C., Vetter, S. & Scheibe, R. (1995) Arch. Biochem. Biophys. **324**, 201-208.

Baalmann, E., Scheibe, R., Cerff, R. & Martin, W. (1996). Plant Mol. Biol. **32**, 505-513.

Bassham, J.A., Benson, A.A., & Calvin, M. (1950). J. Biol.Chem. **185**, 781-787.

Brandes, H. K., Larimer, F. W. & Hartman, F. C. (1996). J. Biol. Chem. **271**, 3333-3335.

Brennich, M. E., Kieffer, J., Bonamis, G., de Maria Antolinos, A., Hutin, S., Pernot, P. & Round, A. (2016). J. Appl. Cryst. **49**, 203–212.

Buchanan, B. B. (1991). Arch. Biochem. Biophys. **288**, 1-9.

Buchanan, B. B. & Wolosiuk, R. A. (1976). Nature. **264**, 669-670.

Carmo-Silva, A. E., Marri, L., Sparla, F. & Salvucci, M. E. (2011). Protein Pept. Lett. **18**, 618-624.

Chiadmi, M., Navaza, A., Miginiac-Maslow, M., Jacquot, J. P., & Cherfils, J. (1999). EMBO J. **18**, 6809-6815.

Del Giudice, A., Pavel, N. V., Galantini, L., Falini, G., Trost, P., Fermani, S. & Sparla, F. (2015). Acta Crystallogr. D Biol. Crystallogr. **71**, 2372-2385.

Emsley, P., Lohkamp, B., Scott, W. G. & Cowtan, K. (2010). Acta Crystallogr D Biol Crystallogr. **66**, 486-501.

Fermani, S., Ripamonti, A., Sabatino, P., Zanotti, G., Scagliarini, S., Sparla, F., Trost, P. & Pupillo, P. (2001). J. Mol. Biol. **314**, 527-542.

Fermani, S., Sparla, F., Falini, G., Martelli, P.L., Casadio, R., Pupillo, P., Ripamonti, A. & Trost P. (2007). Proc. Natl. Acad. Sci. U S A **104**, 11109-11114.

Fermani, S., Trivelli, X., Sparla, F., Thumiger, A., Calvaresi, M., Marri, L., Falini, G., Zerbetto, F. & Trost, P. (2012). J. Biol. Chem. **287**, 21372-21383.

Ferreira-da-Silva, F., Pereira, P. J. B., Gales, L., Roessle, M., Svergun, D. I., Moradas-Ferreira, P. & Damas, A. M. (2006). J. Biol. Chem. **281**, 33433-33440.

Fischer, H., de Oliveira Neto, M., Napolitano, H. B., Polikarpov, I. & Craievich, A. F. (2010). J. Appl. Cryst. **43**, 101-109.

Franke, D., Jeffries, C. M. & Svergun, D. I. (2015). Nat. Methods **12**, 419-422.

Franke, D., Petoukhov, M. V., Konarev, P. V., Panjkovich, A., Tuukkanen, A., Mertens, H. D. T., Kikhney, A. G., Hajizadeh, N. R., Franklin, J. M., Jeffries, C. M. & Svergun, D. I. (2017). J. Appl. Cryst. **50**, 1212-1225.

Gurrieri, L., Fermani, S., Zaffagnini, M., Sparla, F. & Trost, P. (2021). Trends Plant Sci. **26**, 898-912.

Gurrieri, L., Giudice, A. D., Demitri, N., Falini, G., Pavel, N. V., Zaffagnini, M., Polentarutti, M., Crozet, P., Marchand, C. H., Henri, J., Trost, P., Lemaire, S. D., Sparla, F. & Fermani, S. (2019). Proc. Natl. Acad. Sci. U S A. **116**, 8048-8053.

Gütle, D. D., Roret, T., Müller, S. J., Couturier, J., Lemaire, S. D., Hecker, A., Dhalleine, T., Buchanan, B. B., Reski, R., Einsle, O. & Jacquot, J. P. (2016). Proc. Natl. Acad. Sci. U S A. **113**, 6779–6784.

Hajizadeh, N. R., Franke, D., Jeffries, C. M. & Svergun, D. I. (2018). Sci. Rep. **8**, 7204.

Hashimoto, K. & Panchenko, A. R. (2010). Proceedings of the National Academy of Sciences. 107,.

Heyneke, E. & Fernie, A. R. (2018). Biochem. Soc. Trans. **46**, 321-328.

Howard, T. P., Lloyd, J. C. & Raines, C. A. (2011). J. Exp. Bot. **62**, 3799–3805.

Howard, T. P., Metodiev, M., Lloyd, J. C. & Raines, C. A. (2008). Proc. Natl. Acad. Sci. USA. **105**, 4056-4061.

Huppe, H. C., de Lamotte-Guéry, F., Jacquot, J.-P. & Buchanan, B. B. (1990). Planta. **180**, 341-351.

Johnson, M. P. (2016). Essays Biochem. **60**, 255–273.

Konarev, P. V., Volkov, V. V., Sokolova, A. V., Koch, M. H. J. & Svergun, D. I. (2003). J. Appl. Cryst. **36**, 1277-1282.

Krissinel, E. & Henrick, K. (2007). J. Mol. Biol. **372**, 774-797.

Kucukelbir, A., Sigworth, F. J. & Tagare, H. D. (2014). Nat. Methods **11**, 63-65.

Launay, H., Barré, P., Puppo, C., Zhang, Y., Maneville, S., Gontero, B. & Receveur-Bréchot, V. (2018). J. Mol. Biol. **430**,1218-1234.

Lia, A., Dowle, A., Taylor, C., Santino, A. & Roversi, P. (2020) Wellcome Open Res. **5**, 114.

Marri, L., Pesaresi, A., Valerio, C., Lamba, D., Pupillo, P., Trost, P. & Sparla, F. (2010). J. Plant Physiol. **167**, 939-950.

Matsumura, H., Kai, A., Maeda, T., Tamoi, M., Satoh, A., Tamura, H., Hirose, M., Ogawa, T., Kizu, N., Wadano, A., Inoue, T. & Shigeoka, S. (2011). Structure. **19**, 1846–1854.

McFarlane, C. R., Shah, N. R., Kabasakal, B. V., Echeverria, B., Cotton, C. A. R., Bubeck, D. & Murray, J. W. (2019). Proc. Natl. Acad. Sci. U S A. **116**, 20984–20990.

Michelet, L., Zaffagnini, M., Morisse, S., Sparla, F., Pérez-Pérez, M. E., Francia, F., Danon, A., Marchand, C. H., Fermani, S., Trost, P. & Lemaire, S. D. (2013). Front. Plant Sci. **4**, 470.

Minagawa, J. & Tokutsu, R. (2015). Plant J. **82**, 413-428.

Nikkanen, L. & Rintamäki, E. (2019). Biochem. J. **476**, 1159-1172.

Orthaber, D., Bergmann, A. & Glatter, O. (2000). J. Appl Cryst. **33**, 218-225.

Pernot, P., Round, A., Barrett, R., De Maria Antolinos, A., Gobbo, A., Gordon, E., Huet, J., Kieffer, J., Lentini, M., Mattenet, M., Morawe, C., Mueller-Dieckmann, C., Ohlsson, S., Schmid, W., Surr, J., Theveneau, P., Zerrad, L. & McSweeney, S. (2013). J. Synchrotron Rad. **20**, 660-664.

Petersen, J., Teich, R., Becker, B., Cerff, R. & Brinkmann, H. (2006). Mol. Biol. Evol. **23**, 1109-1118.

Petoukhov, M. V., Franke, D., Shkumatov, A. V., Tria, G., Kikhney, A. G., Gajda, M., Gorba, C., Mertens, H. D. T., Konarev, P. V. & Svergun, D. I. (2012). J. Appl. Cryst. **45**, 342–350.

Pettersen, E. F., Goddard, T. D., Huang, C. C., Couch, G. S., Greenblatt, D. M., Meng, E. C. & Ferrin, T. E. (2004). J. Comput. Chem. **25**, 1605-1612.

Pettersen, E. F., Goddard, T. D., Huang, C. C., Meng, E. C., Couch, G. S., Croll, T. I., Morris, J. H. & Ferrin, T. E. (2021). Protein Sci. **30**, 70-82.

Pupillo, P. & Piccari, G. G. (1975). Eur. J. Biochem. **51**, 475-482.

Rambo, R. P. & Tainer, J. A. (2013). Nature. **496**, 477–481.

Reichmann, D. & Jakob, U. (2013). Curr. Opin. Struct. Biol. **23**, 436-442.

Rohou, A. & Grigorieff, N. (2015). J. Struct. Biol. **192**, 216-221.

Roitel, O., Vachette, P., Azza, S. & Branlant, G. (2003). J. Mol. Biol. **326**, 1513-1522.

Scagliarini, S., Trost, P. & Pupillo, P. (1998). J. Exp. Bot. **49**, 1307-1315.

Scheibe, R. & Dietz, K.-J. (2012). Plant Cell Environ. **35**, 202-216.

Scheibe, R., Baalmann, E., Backhausen, J. E., Rak, C. & Vetter, S. (1996). Biochim Biophys. Acta **1296**, 228-234.

Scheres, S. H. W. (2016). Methods Enzymol. **579**, 125-157.

Sparla, F., Pupillo, P. & Trost, P. (2002). Journal of Biological Chemistry. 277, 44946–44952.

Sparla, F., Zaffagnini, M., Wedel, N., Scheibe, R., Pupillo, P. & Trost, P. (2005). Plant Physiol. **138**, 2210–2219.

Stevens, F. J. (1989). Biophys J. **55**, 1155-1167.

Svergun, D. I. (1992). J. Appl. Cryst. **25**, 495-503.

Torres-Bugeau, C. M., Ávila, C. L., Raisman-Vozari, R., Papy-Garcia, D., Itri, R., Barbosa, L. R. S., Cortez, L. M., Sim, V. L. & Chehín, R. N. (2012). J. Biol. Chem. **287**, 2398-2409.

Trost, P., Fermani, S., Marri, L., Zaffagnini, M., Falini, G., Scagliarini, S., Pupillo, P. & Sparla, F. (2006). Photosynth. Res. **89**, 263-275.

Wedel, N. & Soll, J. (1998). Proc. Natl. Acad. Sci. U S A. **95**, 9699-9704.

Wolosiuk, R. A. & Buchanan, B. B. (1978). Arch Biochem Biophys. **189**, 97-101.

Yu, A., Xie, Y., Pan, X., Zhang, H., Cao, P., Su, X., Chang, W. & Li, M. (2020). Plant Cell. **32**, 1556–1573.

Zaffagnini, M., Marchand, C. H., Malferrari, M., Murail, S., Bonacchi, S., Genovese, D., Montalti, M., Venturoli, G., Falini, G., Baaden, M., Lemaire, S. D., Fermani, S., & Trost, P. (2019). Proc Natl Acad Sci U S A **116**, 26057-26065

Zheng, S. Q., Palovcak, E., Armache, J.-P., Verba, K. A., Cheng, Y. & Agard, D. A. (2017). Nat. Methods. **14**, 331-332.

Zimmer, D., Swart, C., Graf, A., Arrivault, S., Tillich, M., Proost, S., Nikoloski, Z., Stitt, M., Bock, R., Mühlhaus, T. & Boulouis, A. (2021) Sci. Adv. **7**, eabi8307.

Zivanov, J., Nakane, T., Forsberg, B. O., Kimanius, D., Hagen, W. J., Lindahl, E. & Scheres, S. H. (2018). Elife. **7**, e42166.

Supporting information

Table S1 Summary of SAXS data acquisition information, sample details, and data analysis software used.

(A) Sample details for the SEC-SAXS experiments			
	inhibited	active-short	active
Loading concentration (mg ml^{-1})	13	11	< 5
Injection volume (µl)	100	200	200
Storage buffer composition	25 mM K-phosphate, pH 7.5, 0.1 mM NAD^+	25 mM K-phosphate, pH 7.5, 5 mM reduced DTT, 20 mM $NADP^+$ 1,3-bisphosphoglycerate*	25 mM K-phosphate, pH 7.5, 5 mM reduced DTT, 20 mM $NADP^+$ 1,3-bisphosphoglycerate*
Elution buffer composition	25 mM K-phosphate, pH 7.5, 0.1 mM NAD^+	25 mM K-phosphate, pH 7.5, 0.1 mM $NADP^+$	25 mM K-phosphate, pH 7.5, 0.1 mM $NADP^+$

*obtained by incubation of phosphoglycerate kinase, 20 U ml^{-1}, with 15 mM 3-phosphoglyceric acid, 10 mM ATP and 5 mM MgCl2

(B) SAXS data collection parameters for the SEC-SAXS experiments	
Source, instrument	ESRF, BM29 (Pernot et al., 2013)
Wavelength (Å)	0.9919
Sample-to-detector distance (m)	2.872
$q=4\pi\sin(\theta)/\lambda$ (2θ scattering angle) range ($Å^{-1}$)	0.005-0.45
Absolute scaling method	water scattering I(0)= 0.01632 cm^{-1}, protein partial specific volume 0.735 cm^3 g^{-1}
Exposure time (s)	1
Capillary path length (mm)	1.8
SEC column	Superdex 200 10/300 GL (GE Healthcare)
Flow rate ($ml \cdot min^{-1}$)	0.5
SEC column temperature (ºC)	22

(C) Sample details for the SC-SAXS experiments		
	inhibited	active
Concentration range (mg ml^{-1})	0.08-1.89	0.1-2.0

Storage and dilution buffer composition	25 mM K-phosphate, pH 7.5, 1 mM NAD^+	25 mM K-phosphate, pH 7.9, 1 mM $NADP^+$

1

(D) SAXS data collection parameters for the SC-SAXS experiments		
	inhibited	active
Source, instrument	ESRF, BM29 (Pernot et al., 2013)	
Wavelength (Å)	0.9919	
sample-to-detector distance (m)	2.872	2.864
q-measurement range ($Å^{-1}$)	0.005-0.45	
Absolute scaling method	water scattering I(0)= 0.01632 cm^{-1}, protein partial specific volume 0.735 cm^3 g^{-1}	
Capillary path length (mm)	1.8	
Injection volume (µl)	50	60
Exposure time (s)	1	2
Number of exposures	10	10
Extra flow time (s)	10	10
Sample temperature (ºC)	4	5

2

(E) Software employed for SAS data reduction, analysis, and interpretation	
Solvent subtraction, averaging and basic analysis (Guinier fit, P(r), Porod Volume)	Matlab scripts, ATSAS 2.8 (Franke et al., 2017)
Theoretical intensity calculations	CRYSOL 3.0, OLIGOMER
Molecular graphics	PyMOL 1.8

3

1 **Table S2** CryoEM data collection and data processing parameters.

DATA COLLECTION	
Microscope model	Thermo Fisher Scientific Tecnai Polara F30
Detector type	GATAN K2 Summit
Imaging mode	Bright field
Accelerating voltage, kV	300
Nominal/Calibrated magnification	31000
Pixel size, Å	1.21
Total exposure time, sec	4
Total Number of collected stacks	2228
Number of stacks used in the analysis	1988
Total dose per stack, $e^{-}/Å^2$	42
Number of frames per stack	40
Defocus range, μm	from -1.5 to -3.5
Defocus step, μm	0.15

DATA PROCESSING, GLOBAL RESOLUTION (Å) AND EMDB ID	
3D reconstruction software package	Relion 3.0
A2B2	
Extracted particles	48558
Refined particles	19636
Symmetry	D2
FSC0.143 (unmasked/masked)	6.5/6.3
Local resolution range, Å	3.7-9.7
EMBD ID	13824
A4B4	
Extracted particles	31023
Refined particles	20777
Symmetry	C1
FSC0.143 (unmasked/masked)	13.1/8.9
Local resolution range, Å	4-15
EMBD ID	13825
A8B8 main conformer	

Extracted particles	64130
Refined particles	23611
Symmetry	C2
FSC0.143 (unmasked/masked)	7.4/5.7
Local resolution range, Å	3.7-10.2
EMBD ID	13826
A8B8 alternative conformer	
Extracted particles	64130
Refined particles	10768
Symmetry	C2
FSC0.143 (unmasked/masked)	8.2/7.1
Local resolution range, Å	4-11.5
EMBD ID	13827
A10B10	
Total extracted particles	33067
Refined particles	7352
Symmetry	C5
FSC0.143 (unmasked/masked)	15.1/13
Local resolution range, Å	4.7-14.7
EMBD ID	13828

1 **Table S3** Detailed summary of the SEC-SAXS data analysis of AB-GAPDH samples.

	inhibited			active-short			active
SAXS frame at injection	90			222			268
Background data							
frames	1-1295			1-1650			1-1886
max VSEC (ml)	10			11.9			13.5
Selected protein data							
frames	1510-1540	1638-1728	1860-1900	1840-1860	1972-2027	2170-2193	2090-2140
VSEC interval (ml)	11.8-12.1	12.9-13.7	14.8-15.1	13.5-13.7	14.6-15.0	16.2-16-4	15.2-15.6
<VSEC> (ml)	12.0	13.3	14.9	13.6	14.8	16.3	15.4
Guinier fit							
Rg (Å)	80.6	66.8	59.6	50.9	39.4	34.0	33.9
σ(Rg) (Å)	1.0	0.1	1.5	0.6	0.1	0.4	0.1
I(0) [kDa c(mg ml^{-1})]	117.9	248.5	16.0	27.2	125.8	23.3	34.0
σ(I(0))	0.5	0.2	0.3	0.3	0.1	0.2	0.1
First q point (Å^{-1})	0.007	0.007	0.013	0.130	0.120	0.220	0.016
Last q point (Å^{-1})	0.016	0.019	0.022	0.025	0.029	0.038	0.038
Auto Rg quality	0.89	0.87	0.96	0.74	0.97	0.99	0.96
Indirect Fourier transform							
Rg (Å)	82.7	66.9	67.2	53.2	40.3	33.9	34.1
σ(Rg) (Å)	0.4	0.1	3.3	0.6	0.1	0.3	0.1
I(0) [kDa c(mg ml^{-1})]	119.3	248.7	16.7	27.6	126.4	23.2	34.2
σ(I(0))	0.4	0.2	0.5	0.2	0.1	0.1	0.1
VP (10^{-3} Å^3)	1100	830	508	346	228	183	201
First q point (Å^{-1})	0.007	0.007	0.013	0.013	0.012	0.022	0.016
Last q point (Å^{-1})	0.25	0.25	0.25	0.25	0.25	0.25	0.25
Dmax imposed for P(r) (Å)	276	217	280	180	146	112	112
Dmax variability estimate (Å)	15	10	25	10	10	5	5
GNOM quality estimate	0.74	0.74	0.65	0.73	0.63	0.75	0.75
MW(VP)[a] (kDa)	647	488	299	203	134	107	118
MW (Vc)[b] (kDa)	712	555	222	208	147	112	132

MW (MoW)[c] (kDa)	681	568	231	225	173	122	148
MW Bayesian[d]							
estimate (kDa)	715	479	318	243	147	119	147
estimate probability (%)	94.6	95.0	79.1	89.0	48.8	46.5	50.4
credibility interval (kDa)	614-751	455-556	221-373	195-264	142-177	111-127	127-151
interval probability (%)	99.8	98.4	99.8	99.6	98.0	92.7	95.9

[a]From the Porod volume VP according to the empirical relation MW~0.625 VP (Petoukhov et al., 2012); [b]From the volume of correlation Vc (qmax for integration 0.25 $Å^{-1}$) (Rambo & Tainer, 2013); [c]From the Porod invariant (qmax for integration 0.25 $Å^{-1}$) (Fisher et al., 2010); [d]From the Bayesian inference approach based on concentration-independent methods (Hajizadeh et al., 2018).

Table S4 Summary of dimensional parameters obtained by the analysis of selected SAXS profiles collected during the SEC elution of AB-GAPDH samples.

		Guinier	P(r)		Porod volume	MW estimate		Possible stoichiometry	
Sample	<VSEC> (ml)	Rg (Å)	Rg (Å)	Dmax (Å)[a]	(10^{-3} Å^3)	MW[b]	MW[c]	MW (kDa)	
inhibited									
	12.0	80.6 ± 1.0	82.7 ± 0.4	270 ± 20	1100	834	715 ± 24	A10B10	741
	13.3	66.8 ± 0.1	66.9 ± 0.1	200 ± 10	830	504	479 ± 20	A8B8	607
	14.9	59.6 ± 1.5	67.2 ± 3.3	180 ± 30	508	266	318 ± 27	A4B4	299
active-short									
	13.6	50.9 ± 0.6	53.2 ± 0.6	170 ± 10	346	208	243 ± 13	A4B4	299
	14.8	39.4 ± 0.1	40.3 ± 0.1	140 ± 20	228	153	147 ± 9	A2B2	149
	16.3	34.0 ± 0.4	33.9 ± 0.3	110 ± 10	183	118	119 ± 6	A2B2	149
active									
	15.4	33.9 ± 0.1	34.1 ± 0.1	100 ± 10	201	134	147 ± 7	A2B2	149

[a]Estimated from the distance value at which the P(r) function calculated from indirect Fourier transform approaches zero; [b]From the Porod volume VP according to the empirical relation MW~0.625 VP (Petoukhov et al., 2012); [c]From the Bayesian inference approach based on concentration-independent methods (Hajizadeh et al., 2018).

Table S5 Cross correlation values for A-subunit or B-subunit positioned in the contact region between adjacent tetramers in the various GAPDH oligomers. The values have been calculated using the "fit" command as implemented in UCSF Chimera (Afonine *et al.*, 2018).

	GAPDH oligomer							
	A4B4		A8B8 Main conf.		A8B8 Alt. Conf.		A10B10	
	A-sub.	B-sub.	A-sub.	B-sub.	A-sub.	B-sub.	A-sub.	B-sub
	0.9416	0.9464	0.9270	0.9334	0.9434	0.9493	0.9744	0.9759
	0.9408	0.9462	0.9270	0.9334	0.9431	0.9493	0.9744	0.9759
	0.9405	0.9449	0.9268	0.9334	0.9411	0.9487	0.9743	0.9758
	0.9397	0.9447	0.9268	0.9326	0.9411	0.9487	0.9743	0.9758
			0.9261	0.9325	0.9406	0.9464	0.9743	0.9758
			0.9260		0.9406	0.9461	0.9743	0.9758
						0.9461	0.9743	0.9758
								0.9758
Average	0.9410	0.9460	0.9270	0.9330	0.9420	0.9480	0.9740	0.9760
SD	0.0008	0.0009	0.0004	0.0005	0.0013	0.0015	0.00005	0.00005
t-test	0.000170926		$5.5205 \cdot 10^{-9}$		$6.80329 \cdot 10^{-6}$		$7.6780 \cdot 10^{-17}$	

1 **Table S6** GAPDH oligomers average interface areas and ΔG calculated by PDBePISA (Krissinel
2 & Henrick, 2007).

GAPDH oligomer	N° Interfaces	Total Interface Area	Single Interface Area	ΔGint	ΔGdiss
	(#)	($Å^2$)		(kcal mol^{-1})	
A4B4	1	656	656	-234.6	35.9
A4B4 (no CTE)	1	403	403	-212.4	-12.4
A8B8 Main Conf.	4	2641	660	-537.9	41.0
A8B8 Main Conf. (no CTE)	4	1795	449	-484.0	-17.0
A8B8 Alt. Conf.	4	2501	625	-732.7	35.5
A8B8 Alt. Conf. (no CTE)	4	1684	421	-668.6	-17.0
A10B10	5	1139	228	-618.6	-34.7

3

4

Table S7 Results of the optimization of the selected averaged SAXS profiles in the SEC-SAXS experiments as a linear combination of AB-GAPDH oligomers. The χ^2 value obtained by fitting the data with a single structural model are reported in the last column for comparison.

			Optimized volume fractions				Calculated			
Sample	<VSEC> (ml)	AB (OR)	A2B2[a]	A4B4	A8B8[b]	A10B10	MW (kDa)	Rg (Å)	χ^2	χ^{2c}
inhibited										
	12.0	-	0	0.154 ± 0.005	0.057 ± 0.008	0.789 ± 0.006	687	77.1	2.4	4.9
	13.3	-	0	0.131 ± 0.001	0.753 ± 0.042	0.116 ± 0.002	591	66.8	4.9	19.2
	14.9	-	0.079 ± 0.176	0.719 ± 0.242	0.162 ± 0.113	0.040 ± 0.035	357	57.8	1.0	1.0
active-short										
	13.6	0	0.114 ± 0.053	0.849 ± 0.069	0.037 ± 0.023	0	294	51.5	1.0	1.0
	14.8	0.146 ± 0.002	0.570 ± 0.002	0.284 ± 0.001	0	0	181	42.2	10.1	143
	16.3	0.332 ± 0.015	0.650 ± 0.013	0.018 ± 0.006	0	0	128	33.0	0.9	1.4
active										
	15.4	0.101 ± 0.007	0.854 ± 0.006	0.045 ± 0.003	0	0	149	34.6	1.1	2.1

[a]From the A2B2 crystal structure (PDB ID 2PKQ) (Fermani et al., 2007); [b]Both the cryoEM derived models of A8B8 were included (main population and alternative conformation) and here the sum of their volume fractions is reported. Their theoretical scattering profile is almost indistinguishable, as seen in Fig. S9; [c]By fitting the selected data with the theoretical scattering profile of a single structural model with CRYSOL 3.0 in fitting mode, as explained in the caption of Fig. S10.

1 **Table S8** Summary of the SC-SAXS data analysis.

Sample	**inhibited**							
Concentration (mg ml^{-1})	1.89	1.52	1.18	0.67	0.52	0.39	0.2	0.08
Guinier fit								
Rg (Å)	82.2	84.6	82.0	81.0	80.8	81.1	80.8	88.9
σ(Rg) (Å)	3.4	4.5	8.7	17.5	20.6	60.0	16.9	11.6
I(0) [kDa]	530	546	513	561	509	490	470	509
σ(I(0))	2	1	1	3	3	4	4	9
First q point (Å^{-1})	0.0075	0.0075	0.0089	0.0099	0.0100	0.0108	0.0080	0.0075
Last q point (Å^{-1})	0.015	0.012	0.015	0.016	0.016	0.016	0.016	0.015
AutoRg quality	0.85	0.78	0.78	0.74	0.71	0.41	0.56	0.42
Indirect Fourier transform								
Rg (Å)	86.0	85.6	86.9	88.2	86.9	88.6	85.6	93.7
σ(Rg) (Å)	0.2	0.3	0.4	0.5	0.8	1.3	1.7	2.3
I(0) [kDa]	536.0	543.5	521.6	581.7	525.1	510.9	477.1	511.6
σ(I(0))	0.9	1.0	1.6	2.3	2.9	4.6	5.7	10.7
VP (10^{-3} Å^3)	1240	1220	1260	1310	1270	1370	1210	1460
First q point (Å^{-1})	0.0075	0.0075	0.0089	0.0099	0.0100	0.0108	0.0800	0.0750
Last q point (Å^{-1})	0.35	0.35	0.35	0.35	0.35	0.35	0.35	0.35
Dmax imposed for P(r) (Å)	340	340	340	340	340	340	340	340
Dmax variability estimate (Å)	50	50	50	50	50	50	50	50
GNOM quality estimate	0.53	0.53	0.53	0.54	0.50	0.52	0.55	0.46
MW(VP)[a] (kDa)	775	763	788	819	794	856	756	913
MW (Vc)[b] (kDa)	626	627	625	619	608	658	607	573
MW (MoW)[c] (kDa)	661	663	658	625	589	687	580	466
Sample	**active**							
Concentration (mg ml^{-1})	2	1	0.5	0.25	0.1			
Guinier fit								
Rg (Å)	66.5	63.0	60.5	54.5	50.2			

σ(Rg) (Å)	1.5	1.0	2.9	2.8	1.5
I(0) [kDa]	134.1	111.6	95.0	76.5	63.7
σ(I(0))	0.2	0.2	0.3	0.3	0.7
First q point ($Å^{-1}$)	0.0097	0.0055	0.0060	0.0060	0.0070
Last q point ($Å^{-1}$)	0.0187	0.0192	0.0187	0.0234	0.0258
AutoRg quality	0.75	0.64	0.82	0.45	0.26
Indirect Fourier transform					
Rg (Å)	70.5	66.6	63.7	59.7	53.9
σ(Rg) (Å)	0.3	0.4	0.6	1.1	2.1
I(0) [kDa]	137.0	113.0	95.8	78.2	64.4
σ(I(0))	0.3	0.2	0.4	0.6	1.1
VP (10-3 $Å^3$)	502	431	363	329	258
First q point ($Å^{-1}$)	0.0097	0.0055	0.0060	0.0060	0.0070
Last q point ($Å^{-1}$)	0.35	0.35	0.35	0.35	0.35
Dmax imposed for P(r) (Å)	300	280	250	240	230
Dmax variability estimate (Å)	100	20	50	30	30
GNOM quality estimate	0.48	0.52	0.46	0.47	0.42
MW(VP)[a] (kDa)	314	270	227	206	161
MW (Vc)[b] (kDa)	312	253	185	168	139
MW (MoW)[c] (kDa)	377	329	219	217	179

[a]From the Porod volume VP according to the empirical relation MW~0.625 VP (Petoukhov et al., 2012); [b]From the volume of correlation Vc (qmax for integration 0.25 $Å^{-1}$) (Rambo & Tainer, 2013); [c]From the Porod invariant (qmax for integration 0.25 $Å^{-1}$) (Fisher et al., 2010).

Table S9 Results of the optimization of the SC-SAXS data for concentration series of active and inhibited AB-GAPDH samples as a linear combination of AB-GAPDH oligomers.

		Optimized volume fractions					Calculated	
Sample	(mg ml^{-1})	A2B2	A4B4	A8B8[a]	A10B10	χ^2	MW (kDa)	Rg (Å)
inhibited	1.89	0	0.163 ± 0.001	0.377 ± 0.002	0.460 ± 0.002	19.1	634	72.6
	1.52	0	0.160 ± 0.002	0.377 ± 0.003	0.463 ± 0.002	13.1	635	72.6
	1.18	0	0.162 ± 0.002	0.362 ± 0.003	0.476 ± 0.003	8.8	636	72.9
	0.67	0	0.161 ± 0.003	0.334 ± 0.005	0.504 ± 0.004	4.8	641	73.3
	0.52	0	0.157 ± 0.004	0.329 ± 0.006	0.513 ± 0.005	3.3	644	73.4
	0.39	0	0.147 ± 0.005	0.307 ± 0.008	0.545 ± 0.007	2.0	652	73.9
	0.20	0	0.146 ± 0.009	0.372 ± 0.016	0.482 ± 0.012	1.0	643	73.0
	0.08	0	0.128 ± 0.023	0.355 ± 0.037	0.517 ± 0.028	0.8	653	73.5
active								
	2.00	0.181 ± 0.011	0.507 ± 0.017	0.042 ± 0.009	0.270 ± 0.003	11.4	412	66.8
	1.00	0.335 ± 0.021	0.445 ± 0.031	0.022 ± 0.016	0.197 ± 0.005	2.2	350	63.5
	0.50	0.453 ± 0.008	0.395 ± 0.009	0	0.152 ± 0.003	1.7	305	60.5
	0.25	0.551 ± 0.016	0.336 ± 0.019	0	0.113 ± 0.005	0.8	272	57.3
	0.10	0.643 ± 0.041	0.283 ± 0.046	0	0.074 ± 0.013	0.8	240	53.1

[a]Both the cryoEM derived models of A8B8 were included (main population and alternative conformation) and here the sum of their volume fractions is reported. Their theoretical scattering profile is almost indistinguishable, as seen in Fig. S9.

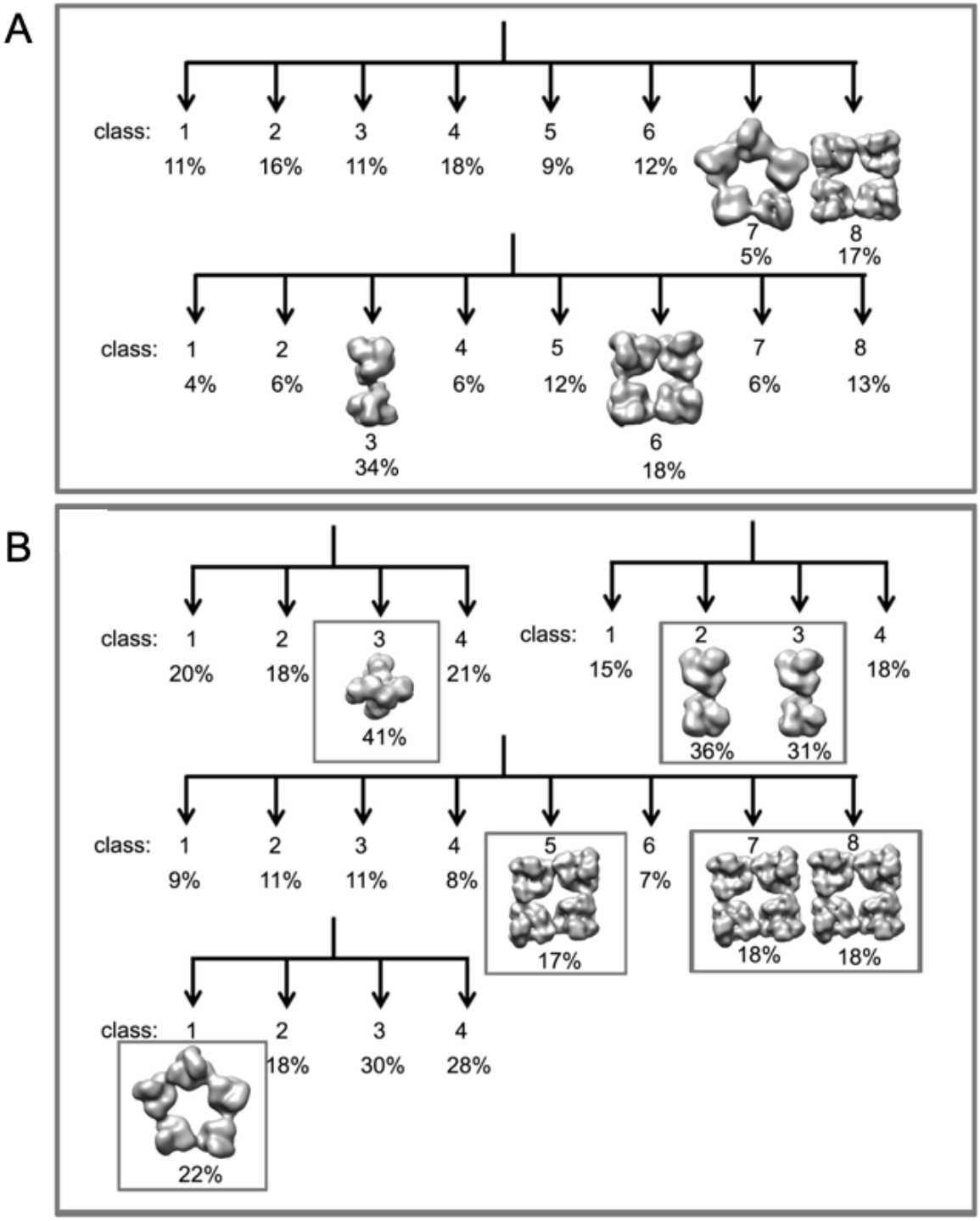

Figure S1 (A) Preliminary 3D classifications performed on the whole GAPDH data set using an ellipsoid (top) and a sphere (bottom) as initial models. (B) 3D classification performed on single GAPDH oligomer data sets. The particles belonging to the boxed 3D classes were used for the final 3D refinement.

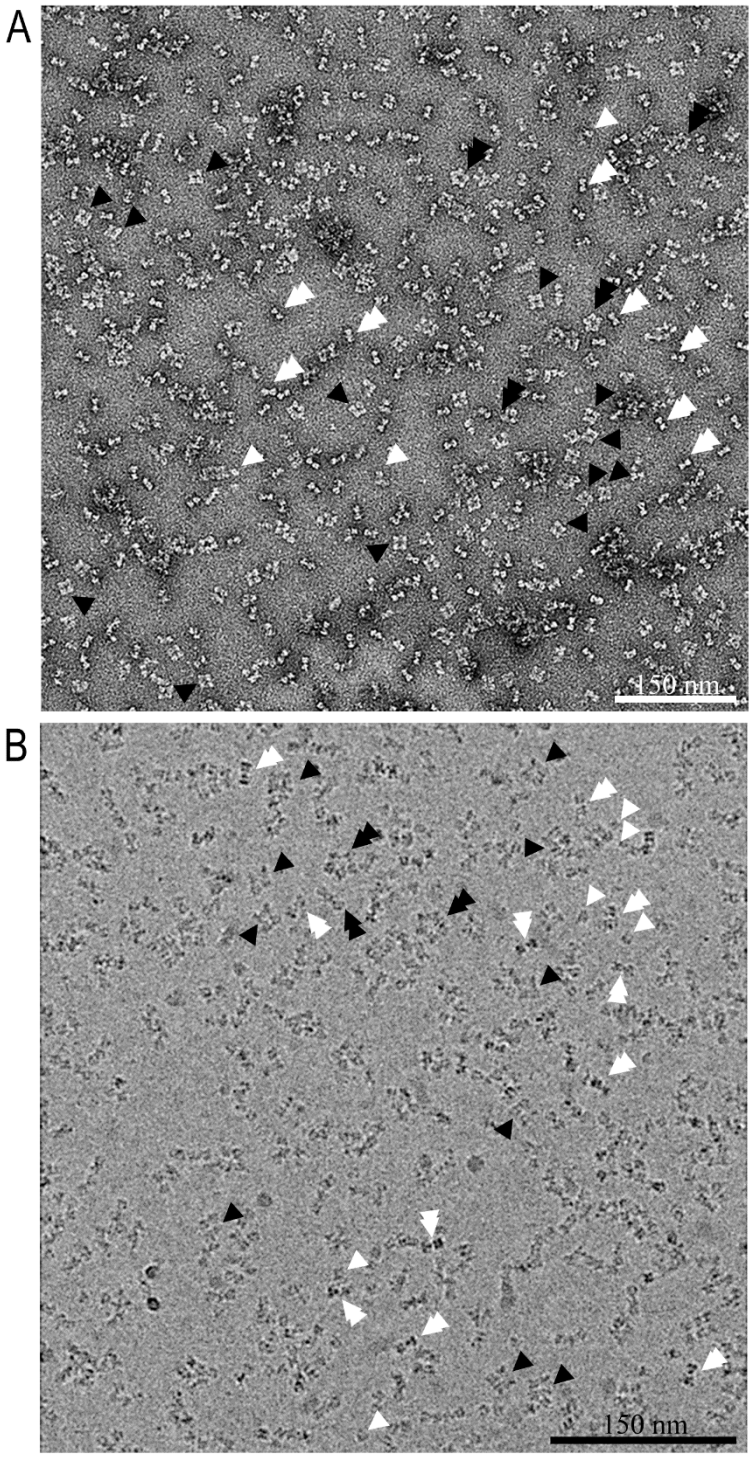

Figure S2 (A) Negative staining and (B) cryoEM representative micrographs. The single and double arrowheads point to the A_2B_2 (single white arrowheads), A_4B_4 (double white arrowheads), A_8B_8 (single black arrowheads) and $A_{10}B_{10}$ (double black arrowheads) projections.

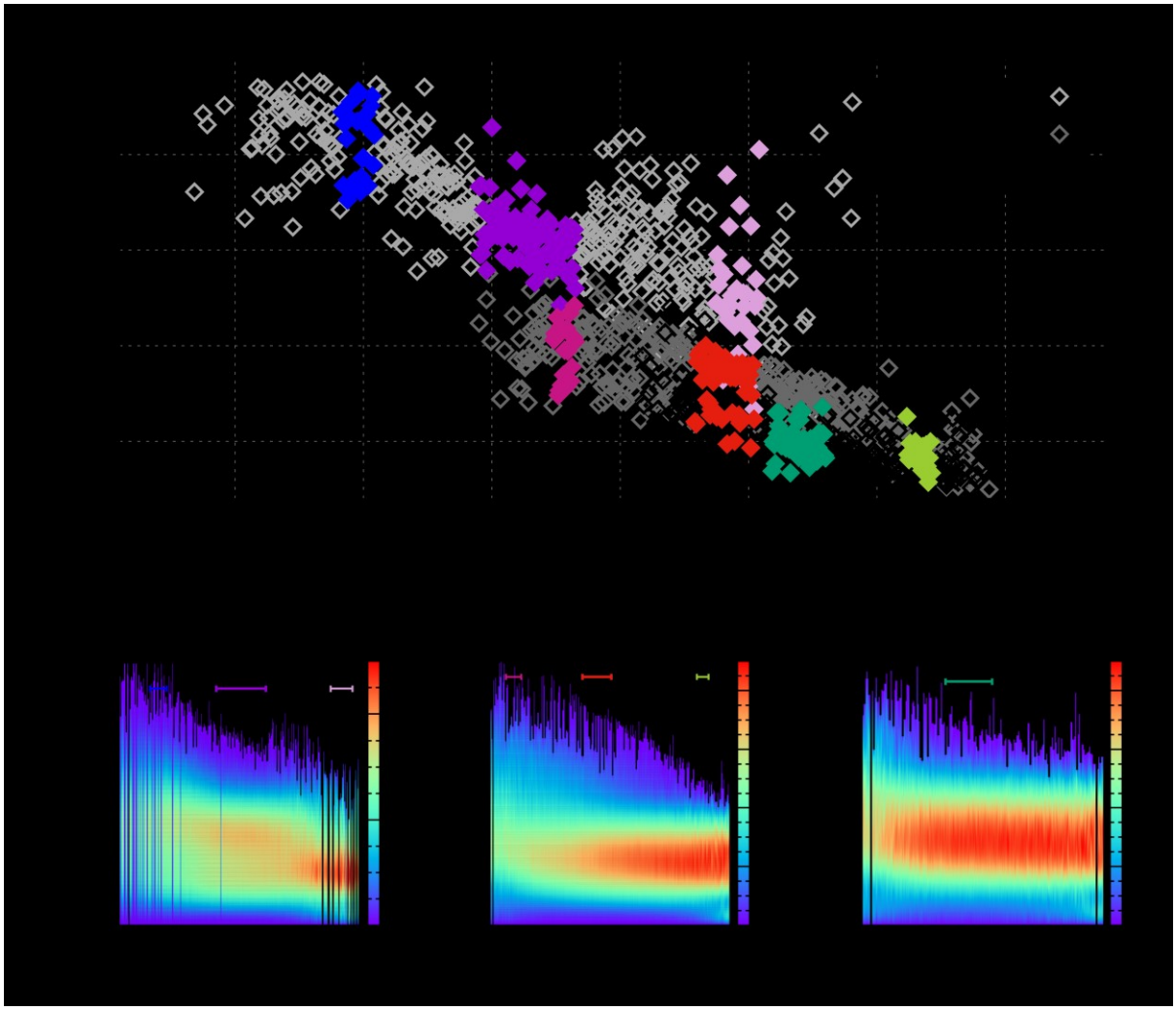

Figure S3 (A) The maximum particle dimension (D_{max}, diamonds) estimated from indirect Fourier transform of the SAXS frames for the three AB-GAPDH samples: inhibited (light grey symbols, maximum at 13 ml), active-short (grey symbols, maximum at 14.8 ml) and active (black symbols, maximum at 15.4 ml), is shown as a function of the SEC elution volume. The data points belonging to the frames averaged to obtain the selected scattering profiles are highlighted with a colour code. 2D maps of (B) inhibited, (C) active-short, (D) active samples analysed by means of SEC-SAXS showing the calculated pair distance distribution function normalized by the subtended area (P(r)/(I(0)), as a function of the SEC elution volume, are presented. The frames averaged to obtain the representative scattering profiles are highlighted by means of bars whose colour key corresponds to that of the plotted P(r) functions in Figure 1.

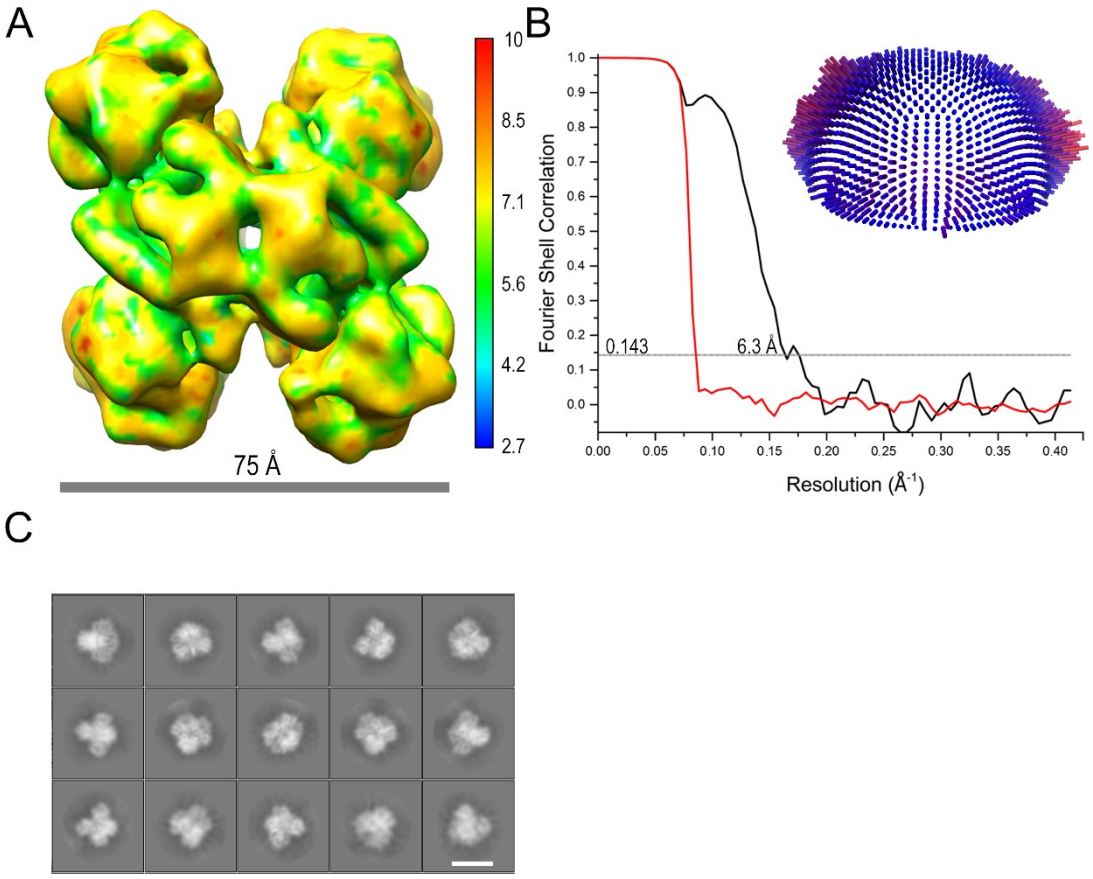

Figure S4 (A) CryoEM electron density map of A_2B_2 oligomer (D2 symmetry) at 6.3 Å resolution filtered according to ResMap local resolution. (B) Fourier shell correlation (FSC) curves (red, FSC phase randomized masked curve; black, FSC corrected curve) of the map with the resolution that corresponds to FSC=0.143 marked. The inset shows the Euler angle distribution. (C) Representative 2D class averages of the A_2B_2 particle images. The scale bar is 80 Å.

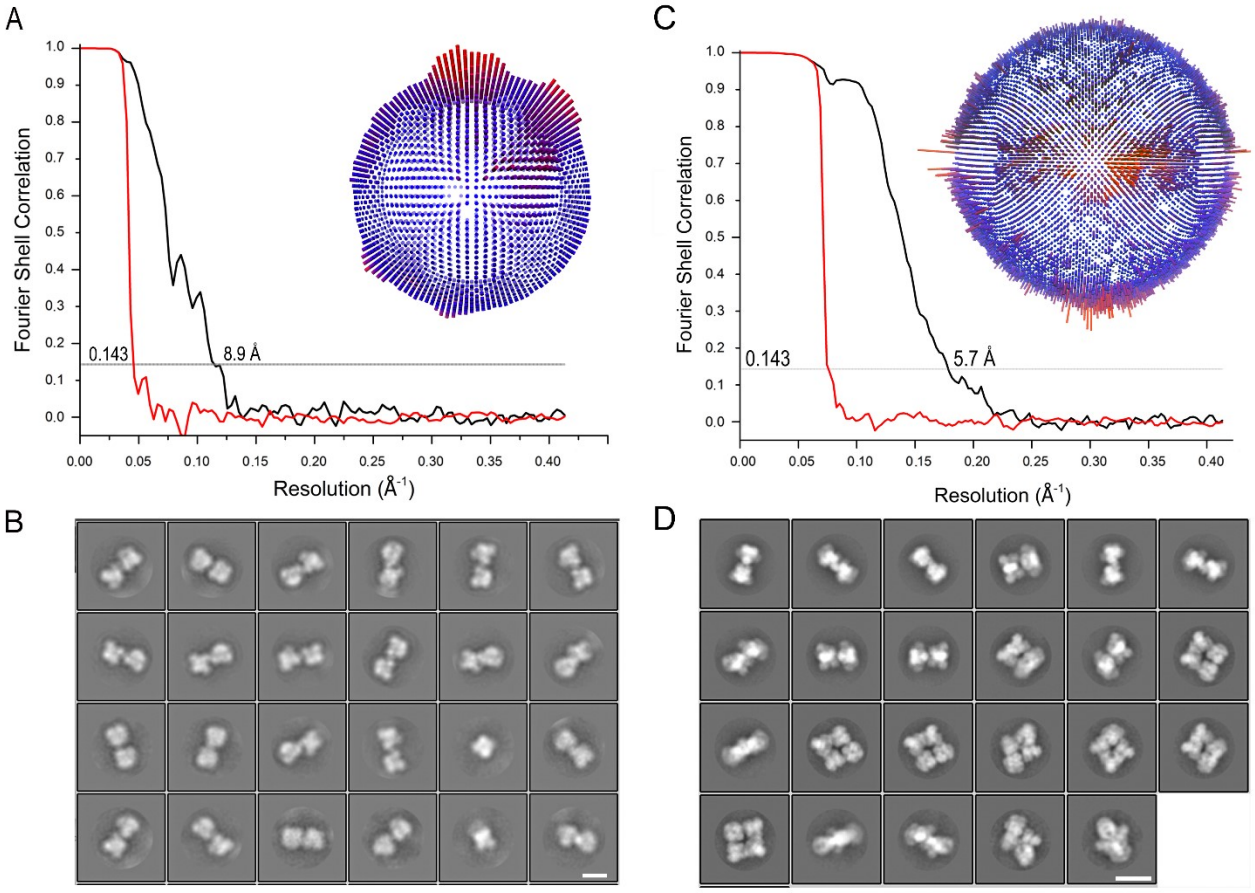

Figure S5 (A) FSC curve of A_4B_4 map (red, FSC phase randomized masked curve; black, FSC corrected curve) with the resolution that corresponds to FSC=0.143 marked. The inset shows the Euler angle distribution. (B) Representative 2D class averages of A_4B_4 particle images. The scale bar is 85Å. (C) FSC curve of the A_8B_8 map (red, FSC phase randomized masked curve; black, FSC corrected curve) with the resolution that corresponds to FSC=0.143 marked. The inset shows the Euler angle distribution. (D) Representative 2D class averages of the A_8B_8 particle images. The scale bar is 150Å.

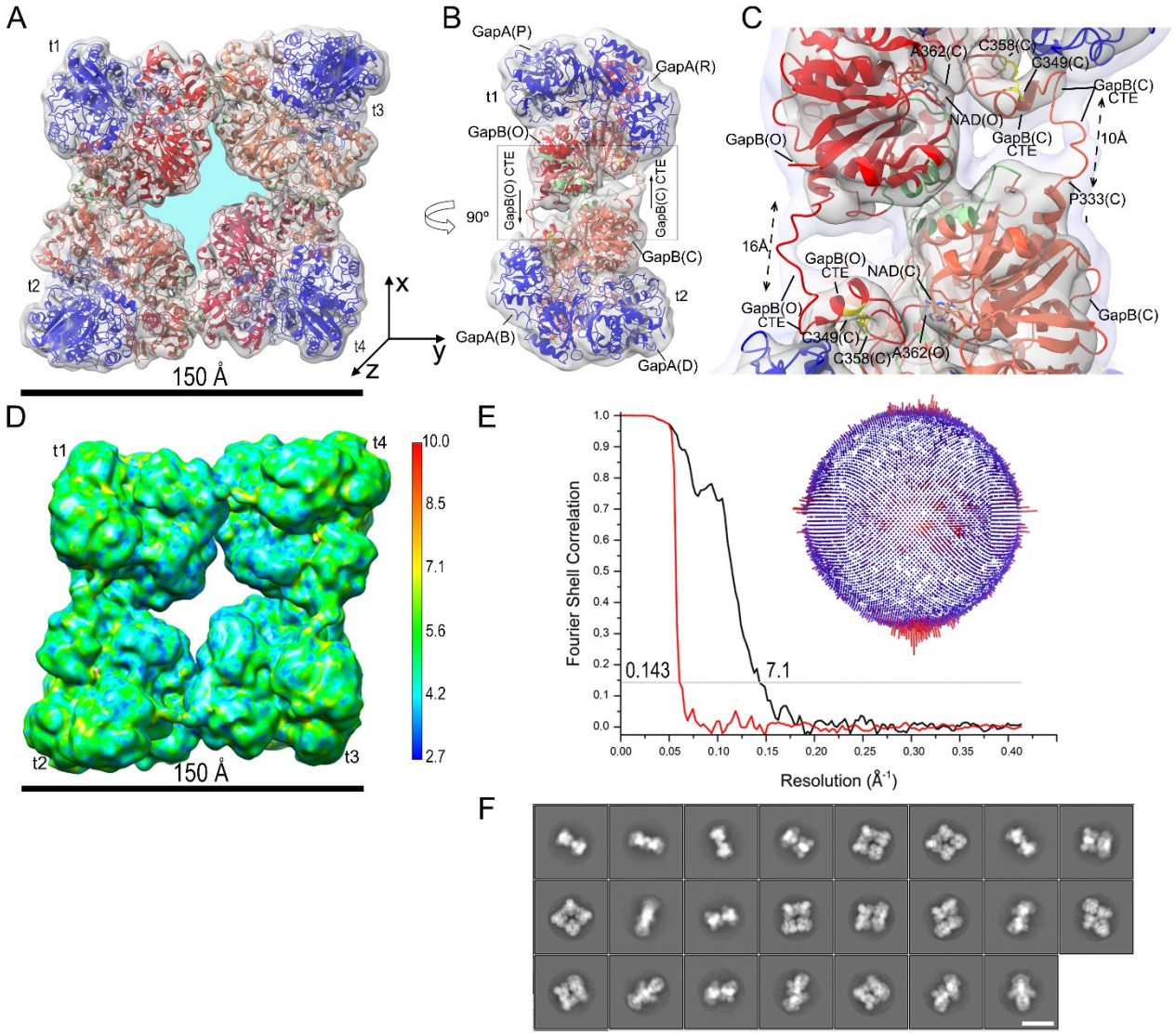

Figure S6 (A) CryoEM electron density map (C2 symmetry) at 7.1 Å fitted with the models derived from the crystal structure of the oxidized A_2B_2 complexed with $NADP^+$ (PDB ID 2PKQ) (Fermani *et al.*, 2007). Labels t1-t4 indicate the A_2B_2 tetramers. The O/Q, A/C, E/G and K/I B-subunits are represented in red, tomato, crimson and coral, respectively. The A-subunits are in blue. The oligomer central cavity (in light blue) has a surface area of 1738 $Å^2$. (B) Side view of the map in (A) shown at low density threshold. (C) Detail of the region boxed in B. The cryoEM electron density map is displayed at two different isosurface levels (high in dark gray and low in light gray). The interfacing residues between adjacent t1 and t2 GAPDH tetramers are highlighted in green. (D) CryoEM electron density map filtered according to ResMap local resolution. (E) FSC curve of the oligomer map (red, FSC phase randomized masked curve; black, FSC corrected curve) with the resolution that corresponds to FSC=0.143 marked. The inset shows the Euler angle distribution. (F) Representative 2D class averages of the A_8B_8 particle images. The scale bar is 150 Å.

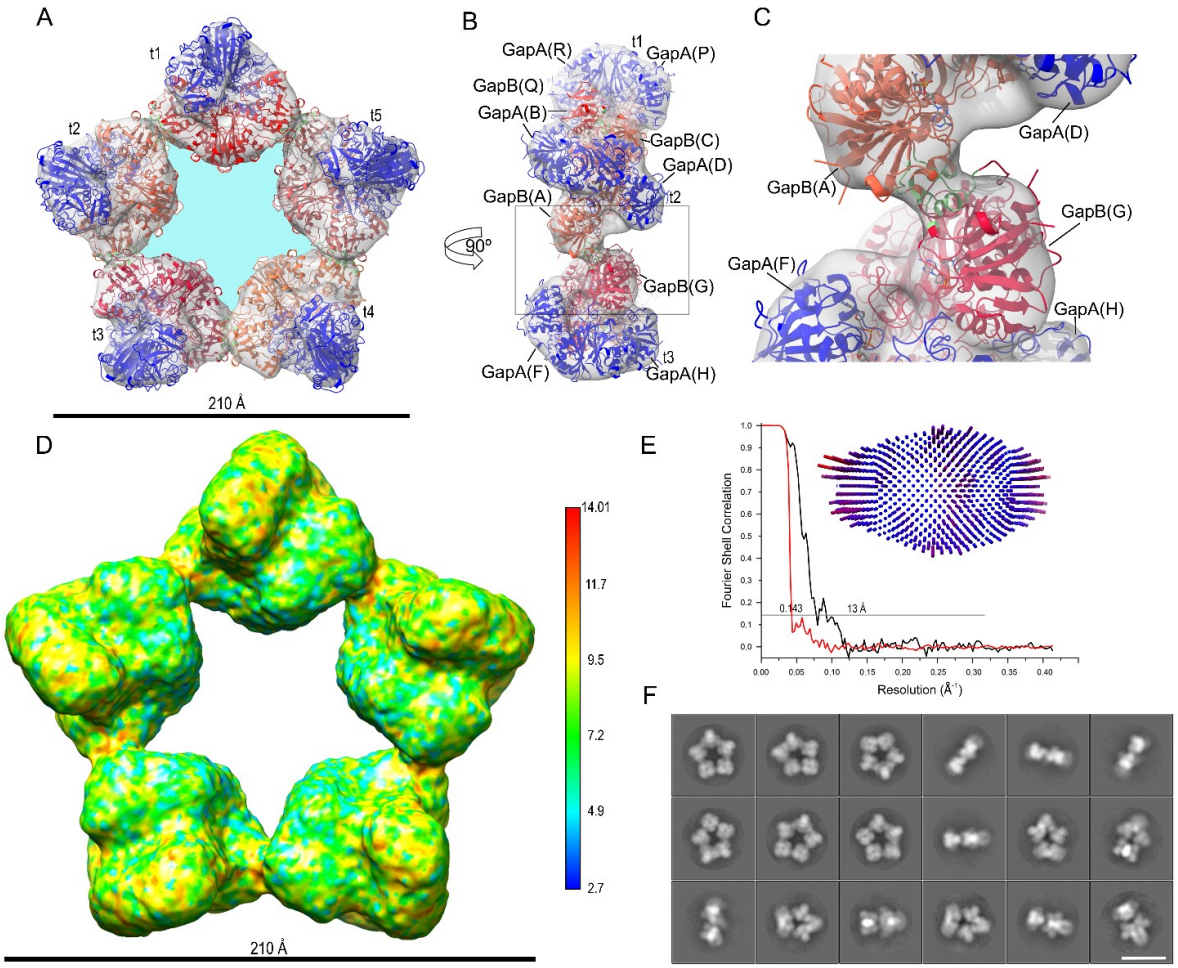

Figure S7 (A) CryoEM electron density map (C5 symmetry) at 13 Å fitted with the models derived from the crystal structure of the oxidized A_2B_2 complexed with NADP+ (PDB ID 2PKQ) (Fermani *et al.*, 2007). Labels t1-t5 indicate the A_2B_2 tetramers. B-subunits are represented in red, tomato, crimson, coral and indian red, while A-subunits are in blue. The oligomer central cavity (in light blue) has a surface area of 5100 $Å^2$. (B) Side view of the map shown in A containing the GAPDH tetramers t1-t3. (C) Detail of the region boxed in B. The interfacing residues between B subunits, i.e. B-subunits (chain A) (tomato) and B-subunits (chain G) (crimson) of adjacent t2 and t3 GAPDH tetramers are highlighted in green. (D) CryoEM electron density map filtered according to ResMap local resolution. (E) FSC curve of the oligomer map (red, FSC phase randomized masked curve; black, FSC corrected curve) with the resolution that corresponds to FSC=0.143 marked. The inset shows the Euler angle distribution. (F) Representative 2D class averages of the $A_{10}B_{10}$ particle images. The scale bar is 200 Å.

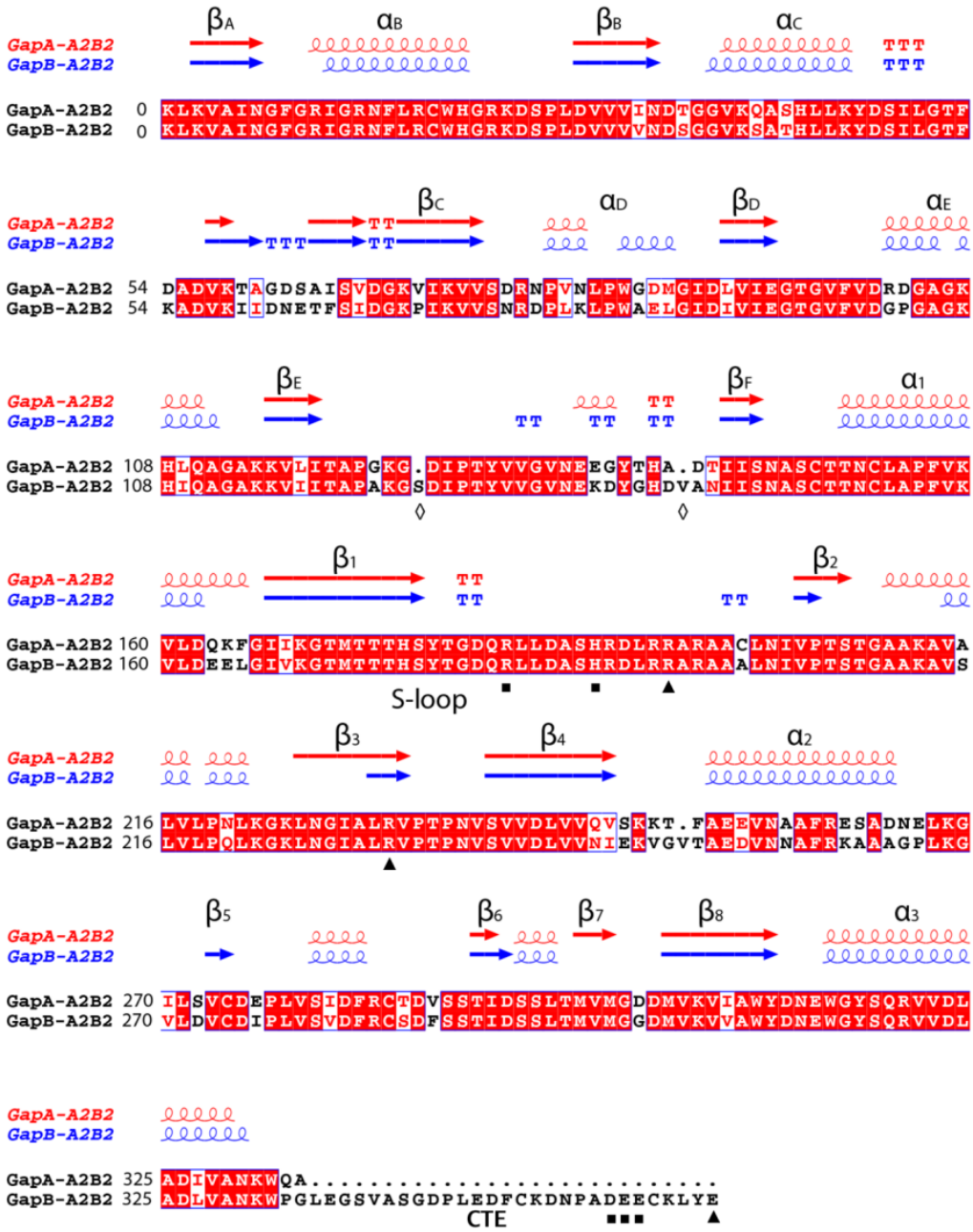

Figure S8 The alignment was performed with ClustalW and visualized with Espript (http://espript.ibcp.fr) using the sequence and the structure of oxidized A_2B_2 B-subunit (chain Q) and A-subunit (chain R) (PDB ID 2PKQ) (Fermani *et al.*, 2007). The black squares and triangles indicate residues likely interacting with CTE residues indicated with the same symbols, of the B subunit belonging to an adjacent tetramer (see main text). White diamonds indicate residue insertions of B-subunit respect to A-subunit.

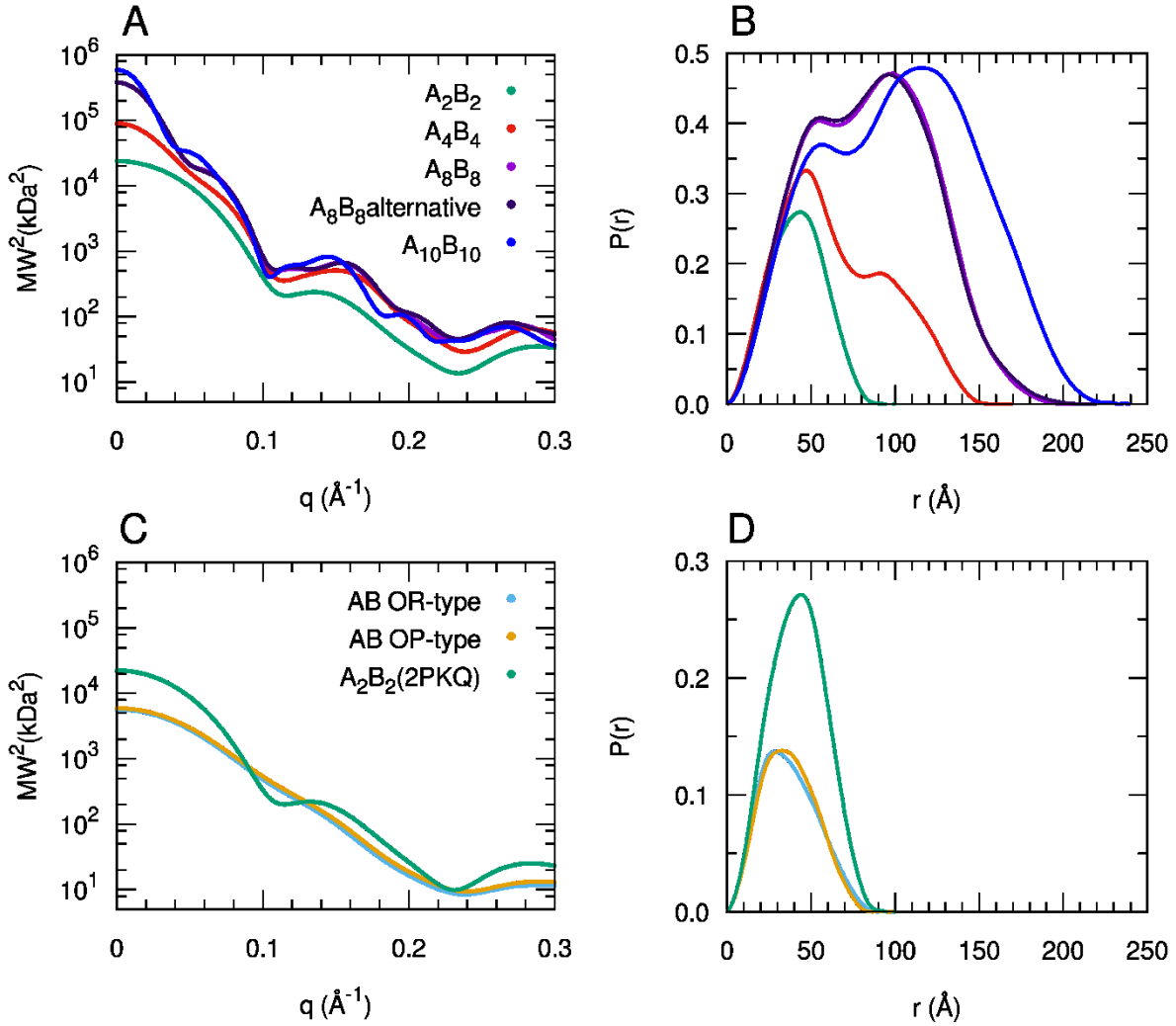

Figure S9 (A) Theoretical scattering profiles calculated from the atomic models of the AB-GAPDH oligomers obtained by cryoEM analysis. In (B) the corresponding pair distance distribution functions (P(r)) provided by indirect Fourier transform of the theoretical profiles are shown. (C) Theoretical scattering profiles calculated from the crystal structure of the AB-GAPDH tetramer in oxidized form complexed with NADP (PDB ID 2PKQ) (Fermani *et al.*, 2007) and from two possible dimeric AB forms. In (D) the corresponding P(r) functions are shown.

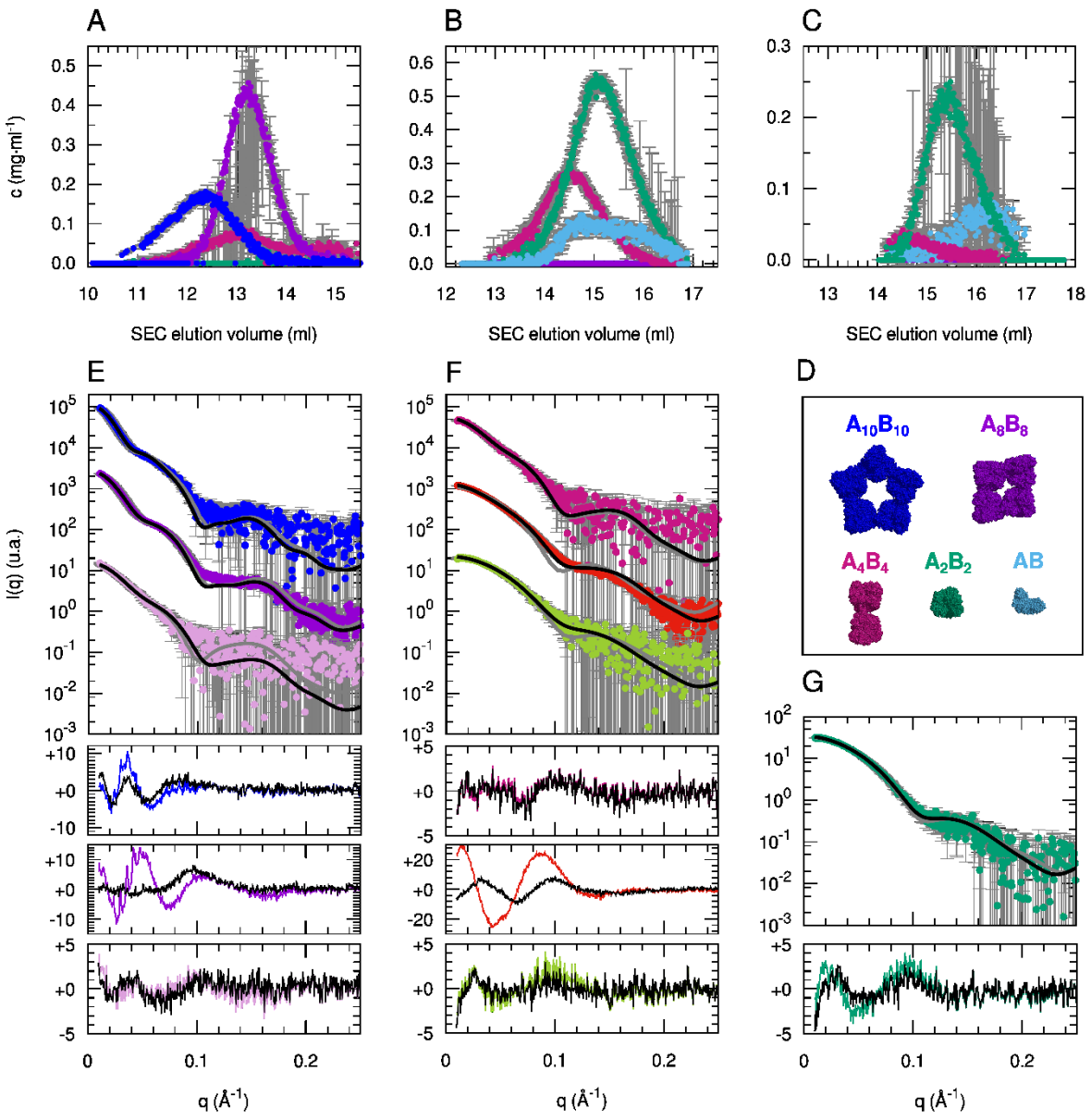

Figure S10 Optimized mass concentrations of the different oligomers as a function of the elution volume (A) for inhibited, (B) for the active-short and (C) for active sample. (D) Color code explanation. (E) Best fit of the three selected average SAXS profiles in the elution of the inhibited sample (blue, violet and pink circles, colour code as in Figure 1A, B) as linear combinations of the AB-GAPDH oligomers $A_{10}B_{10}$, A_8B_8 and A_4B_4 (black lines). The optimized volume fractions are reported in Table S7. The best-fits provided by a single atomic structure ($A_{10}B_{10}$, A_8B_8 and A_4B_4, respectively) are reported as grey lines for comparison. In the panels below error-weighted residual difference plots are reported [$(I_{exp}-I_{calc})/\sigma_{exp}$, where I_{exp} and I_{calc} are the experimental and calculated intensity respectively and σexp are the experimental standard deviations], as black lines for the linear combination fits and as colored lines for the single structure fits. (F) Best fit of the three selected average SAXS profiles in the elution of the active-short sample (purple, red and light green circles, colour code as in Figure 1A, C) as a linear combination of A_4B_4, A_2B_2 or AB (black lines). The best-fits provided by a single atomic

structure (A_4B_4, A_2B_2 and again A_2B_2 respectively) are reported as grey lines for comparison. (G) Best fit of the selected average SAXS profile in the elution of the active sample (green circles, colour code as in Figure 1A, D) as a linear combination of A_4B_4, A_2B_2 or AB (black line). The best-fit provided by a single atomic structure (A_2B_2) is reported as a grey line.

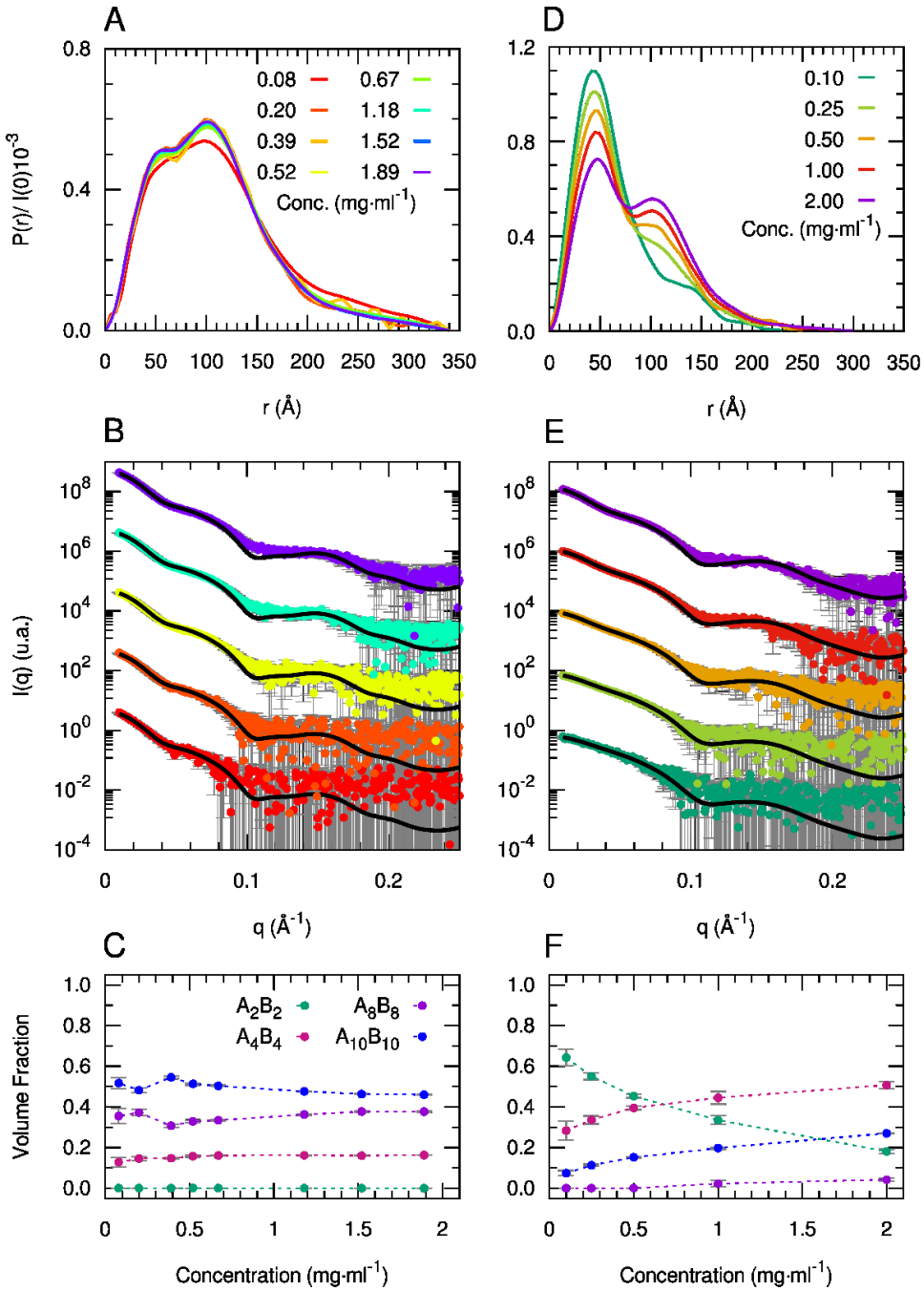

Figure S11 (A) Pair distance distribution functions obtained by indirect Fourier inversion of SAXS data collected on a concentration series of AB-GAPDH incubated in "inhibited" conditions. (B) SAXS profiles of a concentration series of AB-GAPDH incubated in "inhibited" conditions (dots with colour code reported in (A)) and theoretical scattering profiles (black lines) obtained by fitting the data as a linear combination of the form factors calculated from the atomic coordinates of the A_2B_2, A_4B_4, A_8B_8 and $A_{10}B_{10}$ models presented in the manuscript. (C) Volume fractions of the different AB-GAPDH oligomers as a function of protein concentration, obtained from the fitting of SAXS data reported in (B). In panels (D), (E) and (F) the results of the same SAXS data analysis of AB-GAPDH incubated in "active" conditions are reported.

References

Afonine, P.V., Poon, B.K., Read, R.J., Sobolev, O.V., Terwilliger, T.C., Urzhumtsev, A. & Adams, P.D. (2018). Acta Crystallogr. D Struct. Biol. **74**, 531-544.

Fermani, S., Sparla, F., Falini, G., Martelli, P.L., Casadio, R., Pupillo, P., Ripamonti, A. & Trost P. (2007). Proc. Natl. Acad. Sci. U S A **104**, 11109-11114.

Fischer, H., de Oliveira Neto, M., Napolitano, H. B., Polikarpov, I. & Craievich, A. F. (2010). J. Appl. Cryst. **43**, 101-109.

Franke, D., Petoukhov, M. V., Konarev, P. V., Panjkovich, A., Tuukkanen, A., Mertens, H. D. T., Kikhney, A. G., Hajizadeh, N. R., Franklin, J. M., Jeffries, C. M. & Svergun, D. I. (2017). J. Appl. Cryst. **50**, 1212-1225.

Hajizadeh, N.R., Franke, D., Jeffries, C.M. & Svergun, D. I. (2018). Sci. Rep. **8**, 7204.

Krissinel, E. & Henrick, K. (2007). J. Mol. Biol. **372**, 774-797.

Pernot, P., Round, A., Barrett, R., De Maria Antolinos, A., Gobbo, A., Gordon, E., Huet, J., Kieffer, J., Lentini, M., Mattenet, M., Morawe, C., Mueller-Dieckmann, C., Ohlsson, S., Schmid, W., Surr, J., Theveneau, P., Zerrad, L. & McSweeney, S. (2013). J. Synchrotron Rad. **20**, 660-664.

Petoukhov, M. V., Franke, D., Shkumatov, A. V., Tria, G., Kikhney, A. G., Gajda, M., Gorba, C., Mertens, H. D. T., Konarev, P. V. & Svergun, D. I. (2012). J. Appl. Cryst. **45**, 342–350.

Rambo, R. P. & Tainer, J. A. (2013). Nature. **496**, 477–481.